UNIVERSIDAD DE CHILE
FACULTAD DE CIENCIAS FÍSICAS Y MATEMÁTICAS
DEPARTAMENTO DE INGENIERIA ELECTRICA

IDENTIFYING CONDUCTANCE PATHWAYS IN SINGLE PORPHYRIN MOLECULES

TESIS PARA OPTAR AL GRADO DE MAGISTER EN CIENCIAS DE LA INGENIERIA, MENCION ELÉCTRICA

MEMORIA PARA OPTAR AL TITULO DE INGENIERO CIVIL ELÉCTRICO

ALFREDO RATES SORIANO

PROFESORA GUÍA :
DIANA DULIC

PROFESOR CO-GUÍA :
HERRE S.J. VAN DER ZANT

MIEMBROS DE LA COMISIÓN:
MARCOS ORCHARD CONCHA
MÓNICA SOLER JAUMA

Este trabajo ha sido parcialmente financiado por la Unión Europea a través de un proyecto RISE (DAFNEOX), SEP 210165479 y por el proyecto Fondecyt Regular número 1181080.

SANTIAGO DE CHILE
2019

RESUMEN DE LA MEMORIA PARA OPTAR
AL TÍTULO DE INGENIERO CIVIL ELECTRICO
POR: ALFREDO RATES SORIANO
FECHA: 2019
PROF. GUÍA: DIANA DULIC HERRE S.J. VAN DER ZANT

IDENTIFYING CONDUCTANCE PATHWAYS IN SINGLE PORPHYRIN MOLECULES

La utilización de moléculas aisladas como componentes electrónicos es una idea fascinante que ha atraído la atención de múltiples áreas de la física esta última década. Pero la capacidad de controlar el transporte de cargas a través de dichas moléculas depende fuertemente en nuestro conocimiento de sus mecanismos de conductividad y del sendero que recorren las cargas al interior de las moléculas. Con el motivo de estudiar este fenómeno, se midieron exhaustivamente siete diferentes derivativos de porfirinas con estructuras similares.

Para medir la conductancia de de moléculas aisladas de porfirina se utilizó la técnica de ruptura de juntura mecánicamente controlada (MCBJ por sus siglas en inglés). Esta técnica utiliza nano-dispositivos fabricados mediante litografía en el cual un puente de oro de 100 nm de ancho queda suspendido al centro de la muestra. Esta es flexionada con el fin de quebrar y, luego, unir el cable de oro, formando nano-electrodos en los extremos de este. Con esta técnica, una molécula puede ser atrapada para luego medir la corriente a través de esta.

Decenas de miles de curvas de conductividad fueron medidas. Para el análisis de estos datos se utilizó un algoritmo de clasificación imparcial basado en aprendizaje de máquinas, en particular se utilizó el algoritmo K-Means, el cual hace uso de la distancia o correlación de cada evento para clasificar las mediciones en diferentes clases. Al aplicar este método en nuestro experimento se pudieron relacionar los diferentes valores de conductividad medidos con rutas específicas dentro de la molécula por la cual las cargas pueden fluir.

La correlación entre la presencia de cada clase en porfirinas con bloques estructurales similares permitió su asignación la ruta correspondiente. Con la serie de porfirinas medidas se pudieron distinguir tres diferentes rutas de conductividad en un rango mayor a cuatro órdenes de magnitud. La primera y principal corresponde a la molécula completamente extendida, de manera tal que la conductividad se maximiza. Otras clases con menor conductividad fueron observadas y se atribuyeron a la presencia de grupos espaciadores fenileno-acetileno en la molécula.

ABSTRACT OF THE THESIS TO OBTAIN
THE TITLE OF ELECTRICAL ENGINEER
BY: ALFREDO RATES SORIANO
DATE: 2019
SUPERVISOR: DIANA DULIC HERRE S.J. VAN DER ZANT

IDENTIFYING CONDUCTANCE PATHWAYS IN SINGLE PORPHYRIN MOLECULES

Using single molecules as electronic components for a new generation of electronic devices is a fascinating idea that has attracted attention from many fields in science during the last decade. However, the ability to control transport in single molecule devices depends heavily on our understanding of the conductivity and charge pathway inside these molecules. To study this phenomenon, for this thesis seven structurally related porphyrin derivatives were repeatedly measured.

To measure single porphyrin molecules, the mechanically controlled break-junction technique was used. This technique is based on lithographically fabricated devices with a gold wire and a suspended constriction 100 nm wide that can be bent in order to break and make the wire, forming nano-sized gold electrodes. With this technique, a single molecule can be attached and we can measure its conductance.

Tens of thousands of conductance traces were measured. To analyze these measurements, an unbiased clustering algorithm was used. This algorithm is based on the K-means algorithm, which can classify the data into different categories using the distance or correlation of all the events. By applying this to our data we were able to link the different conductance values extracted from the conductance measurements to the corresponding electron paths.

The correlation between the appearances of similar classes in particular sub-sets of the porphyrins with a common structural motif allowed to assign the corresponding current paths. The series of model porphyrins allowed to identify and distinguish three different electronic paths covering more than four orders of magnitude in conductance. The first path corresponds to the fully stretched molecule that gives the highest conductance. Other classes with lower conductance were found and were related to the presence of phenylene-acetylene spacers in the molecule.

A mi familia, a mis amigos y a ti,

que por alguna razón

estás leyendo mis escritos.

Acknowledgements

First, I want to thank prof. Diana, without her, nothing of this would be real. Thank you for trusting me to work with you. I also want to thank prof. Herre to accept me in his group and take part in his research. Thank you for all you taught me and for all the good moments in the lab!

Debo agradecer también a mi familia, con quienes he compartido desde que nací. Gracias a mi madre Pamela y a mi padre Alfredo por todo el apoyo que me han brindado. Gracias a mis hermanos Miguel y Nené, los quiero mucho. Quiero agradecer también a mi hermano Diego por recibirme con tanto cariño en Edimburgo y a mi tía Marcela por su ayuda y apoyo en mi viaje.

De la universidad hay mucha gente a la que debo agradecer. Del laboratorio de fotónica debo agradecer a Ernest por aceptarme en él. Además, agradecer a todos con los que trabajé. En particular a Nico alias Villano circunstancial y Nico alias El Capitán. Gracias por todo el apoyo y buena onda que sigue hasta el día de hoy. Del laboratorio de Electrónica Molecular agradecer a Cristian por lo que me enseñó y en particular a Jacqui, quien me ayudó muchísimo tanto en el laboratorio como en la carrera y mi viaje a Delft. Y no podría olvidarme de Danny y Felipe, quienes me han escuchado y apoyado durante todo este tiempo desde el inicio de mi carrera. Espero que nuestra amistad e mantenga pese al tiempo y la distancia.

And last but not least, all the people I met in Delft. Of course all the people from van der Zant lab, who accepted me as I am. In particular thanks to *the gang*; Luca, you are a fantastic person. Please, never change your humor! keep running and I hope you enjoy your PhD in Delft. Chunwei, thanks for all the talks, I know you are in tears right now but don't worry, I'll see you soon in SSBU online. And Davide (who I'm sure is checking all my grammar errors even in Spanish) thank you for all you taught me, not only in the lab but in life. You are an amazing person and remember the only limit you have, is that you think you have a limit. And finally Maria, ayayai Maria Maria. Thank you for everything. There is so much you did for me, that even if I thank you for one hundred pages it won't be enough. You are a wonderful person, but don't forget to think about yourself. You deserve it.

Pero si hay alguien a quien realmente debo agradecer, es a la Cata, mi compañera de vida. Gracias por todo. Gracias por ayudarme a estudiar, incentivarme con mis proyectos personales y en general a ser una mejor persona. All I gotta do is thank you girl, thank you girl.

Contents

Chapter 1

Introduction

1.1 Motivation

Single molecular electronics is the field that studies charge transport through single molecules or a few molecules in parallel. The field aims to exploit the functionalities of the molecules in order to use them as electronic components. Because of the nanometer size of single molecules, the field of molecular electronics is promising not only for application but also to study the fundamental laws that govern quantum transport in these nano-scale systems. However, for the same reason, the experimental measurements and modeling of molecular systems are difficult to achieve, as they are too small to study with classical mechanics but too big to simulate in all details using ab-initio, quantum mechanical methods.

1.1.1 History and current challenges

The field of molecular electronics was born in 1971 when Kuhn and Mann [1] measured the conductivity of molecular monolayers. That same decade, Aviram and Ratner [2] attracted the attention to the field as they proposed that a single molecule can work as an electronic rectifier. This theoretical interest could not be proven experimentally until 20 years later with the invention of the scanning tunneling microscope (STM) when the conductance of the first single molecule was measured by Joachim and Gimzewsky [3], followed by Mark Reed and co-workers [4] using the mechanically controllable break-junction (MCBJ) technique. After that, the field of molecular electronics has grown incredibly and single molecules have been integrated into, among others, optical detectors [5], electrochemical switches [6] and photo-voltaic cells [7]. The study of molecular electronics also influences other areas such as electronics and photonics, with applications in conducting polymers, organic superconductors, electrochromic, and more [8].

Nevertheless, significant challenges remain in the field [9] as key aspects of conductance like the junction geometry or the molecule configuration can not be fully predicted. Some examples of these challenges are reproducibility, the lack of control in contacting the molecules and

discrepancy between theory and experiments, showing that there are still many interesting questions to answer before applications of single molecules as electronic components.

1.2 Porphyrins: the *molecular* part of molecular electronics

Porphyrins are organic and aromatic molecules based on the molecular compound *porphine*. They are found widely in nature, being of vital importance in biological systems. Some examples are the chlorophyll in plants, hemoglobin and B12 vitamin in animals, bacteriochlorophyll in some bacterias and petroporphyrin in petrol and sediments [10].

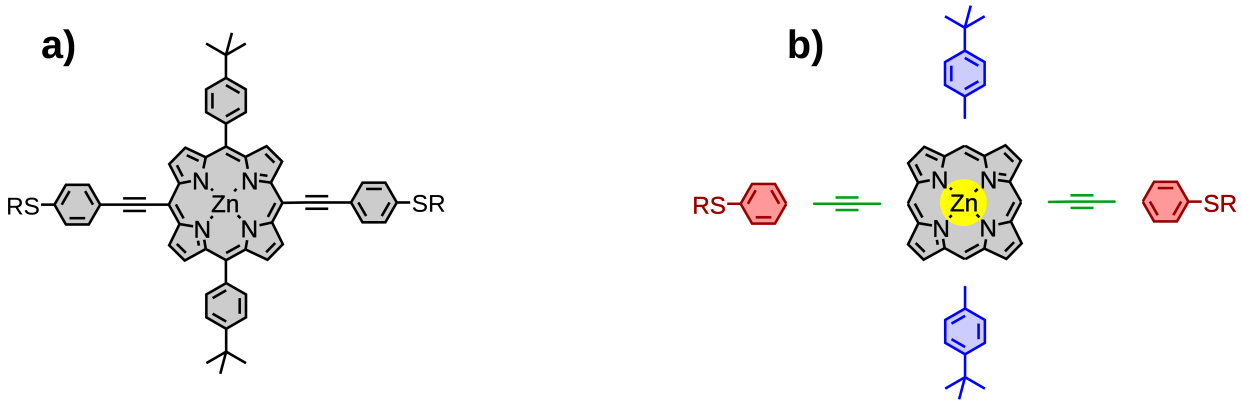

Figure 1.1: **a)** Molecular structure of a porphyrin and **b)** the different modules. The porphyrin consists of the porphine ring (grey), the core (yellow), spacer groups (green), bulky groups (blue) and anchoring groups (red).

Porphyrins are attractive for molecular electronics because their synthesis is well established, allowing to tune their chemical structure [11]. In a modular way porphyrins can be seen as depicted in Fig. 1.1, where we identify the porphine ring (coloured grey in the figure), the core of the porphyrin where a metal ion (yellow) can be placed and side groups where anchoring groups (red) can be used to attach the molecule to the leads and bulky groups (blue) to prevent this attachment or spacer groups (green) as intermediate groups. The porphine is the part that all molecules called porphyrins have in common, while the other parts can be chosen in diverse combinations to obtain similar but yet different molecules. All these combinations can be used to study the relation between the chemical structure of the molecule and its electronic properties in a molecular junction.

1.2.1 State of the art

In previous studies, some of these combinations have been put to the test. Multiple studies [12–16] measured the conductance of different porphyrins forming chains of various sizes in

order to find the length dependence of the conductance. This has been found to follow the relation $\sigma \propto e^{-\beta L}$, where σ is the conductance, L is the chain length and β is the attenuation factor of the conductance per units of length. These studies show that porphyrins have an ultra-low attenuation β factor [17] or even a positive β factor in some cases [18], positioning the porphyrins as good candidates for molecular wires.

Studies have also focused on changing different parts of the molecule to increase or stabilize the conductance of the porphyrins, including different metal centers [19], anchoring [20] or bulky groups [21]. Similarly, other studies tried to identify the charge pathways inside the porphyrins, changing the injection points [22] or comparing parallel with perpendicular stacking [23]. These works compared the conductance and stability in each case, finding that adding anchoring groups like thiol groups (-SH) increases the stability while inserting metal ions like copper (Cu) can increase the conductance up to a factor of 2. Nevertheless, since multiple configurations are possible, the experiment has shown a large spread in conductance values. Because of that, the different conductance pathways through the molecule were not identified and further studies are needed.

1.3 Hypothesis

Porphyrins have multiple functionalities that can be used in molecular electronics, like chemical stability, light absorption and ultra-low attenuation factors for electronic transport. To take advantage of these functionalities, it is important to have high stability and a high conductance in the molecular junction. The stability is mainly affected by the structure of the molecule and the injection point of the charges, while the conductance depends on the contact-molecule interface and the pathways of charges movement inside the molecule. Thus, changing the bulky groups allows us to modify the structure of the molecule, where we expect to have a more stable molecular junction with planar structures. Next, adding anchoring groups to the molecule can increase both the stability and the conductance as the molecule is better attached to the contacts. We expect the molecules with thiol groups to have better stability than without this anchoring group. Finally, the spacer groups and the presence of a metal in the core of the molecules can affect the conductance depending on the charge pathway.

1.3.1 Objectives

In this thesis, porphyrin molecules were measured using the MCBJ technique. This study aimed to compare the conductance of different porphyrins with the same central part in order to identify the conductance pathways.

Specific objectives

- Understand how to use the MCBJ technique to measure the conductance of stable single-porphyrin junctions.
- Learn to fabricate nano-devices to be used in the MCBJ set-up.
- Analyze the measured data with clustering methods based on machine learning algorithms.
- Interpret the data and draw conclusions from it, identifying the conductance pathways in porphyrin molecules and how these are affected by changing the different modules of the molecule like anchoring groups, bulky groups and incorporating metal ions in the core.

1.3.2 Document structure

In the following chapters, first a theoretical approach to transport at the nano-scale will be presented (chapter 2), particularly the electronic transport in single molecule junctions. Then, the clustering method used will be explained (chapter 4)along with the limits of the algorithm and the followed procedure. Next, the measurement of every molecule will be shown (chapter 5), followed by the corresponding interpretations and the results of the clustering analysis (chapter 6). Finally, the conclusions and the last remarks are presented (chapter 6.4)

Chapter 2

Theory

In this chapter, the conductance mechanisms of a molecular junction are described. These depend strongly on the dimensions of the system; the main ones to consider are the size of the conductor, the Fermi wavelength and the elastic and inelastic mean free path.

The size of the conductor corresponds to the physical dimension of the device in the x, y and z-direction (L_x, L_y and L_z respectively). The Fermi wavelength λ_f, on the other hand, arises from the wave-like behavior of the electrons and is defined as the wavelength of the electron with the highest energy of the system. The other two lengths are the elastic and inelastic mean free path (l_{e} and l_ϕ), corresponding to the average length in which an electron can travel before an elastic or inelastic scattering event occurs, respectively. When an elastic scattering event occurs, the electron energy and the phase are conserved; alternatively, in an inelastic scattering event, the energy is not conserved and the information about the phase is lost.

For the case of a molecular junction with gold contacts, when the temperature (T) is near the absolute zero, the Fermi wavelength in the gold contacts is $\lambda_f \sim 0.5$ nm. Depending on the molecule, the size of the system $L_{x,y,z}$ can range between a few angstroms to a few nanometers, while the elastic and inelastic mean free paths of the Au leads are of the orders of tens of nanometers [24, 25]. These values are strongly related to environmental variables; a higher temperature leads to a shorter l_ϕ and a higher number of impurities or vacancies in the material decreases l_{e}. The scenario described above corresponds to the *quantum ballistic regime* of transport as $\lambda_f \sim L_{x,y,z} < l_{\mathrm{e}} < l_\phi$. In this case, the electron can travel from one side of the system to the other without undergoing neither elastic nor inelastic scattering. Thus, the conductance does not depend on the length of the system and there is no dissipation on the wire, which occurs only in the Drain contact.

2.1 Scattering formalism

In this section, we calculate the current through a nano-size contact using the scattering formalism. The schematic of the device is presented in Fig. 2.1.a and 2.1.b, where the

quantum wire is connected between two electrodes with or without a scattering region in the center. In Fig. 2.1.c the energy state diagram is shown when a fixed bias is applied to the quantum wire without scattering.

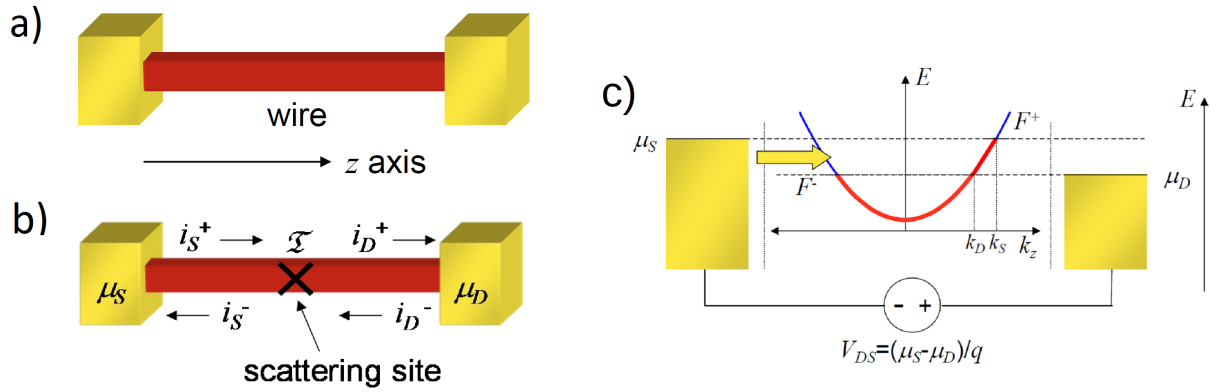

Figure 2.1: Schematic of the system for the case of an ideal quantum wire **a)** without and **b)** with a scattering site in the center. **c)** the energy state distribution diagram of the quantum wire presented in **a)** when multiple energy levels are considered. Figures extracted fro Ref. [26]

In the ideal one-channel case without scattering nor reflected charges, we can model the molecular junction as a quantum wire between two reservoirs like in Fig.2.1.a with a transparent scattering region, where the electrons can move freely in the z-direction but are confined in the other two dimensions. If the chemical potentials of the source and drain are the same ($\mu_S = \mu_D$), there is no current through the system. But if a bias $V = (\mu_S - \mu_D)/e$ is applied between both contacts, a current can flow through the quantum wire from source to drain. At zero temperature, the total current is given by [26]

$$I = e \cdot N/\tau, \tag{2.1}$$

where N is the number of electrons and τ is the transit time, defined as the time required to cross the quantum wire from one reservoir to another. The transit time is expressed as

$$\begin{aligned} \tau &= L_z/v, \\ \text{with } v &= \frac{1}{\hbar} \cdot \frac{\mathrm{d}E}{\mathrm{d}k}. \end{aligned} \tag{2.2}$$

Here, L_z is the length of the quantum wire, v is the group velocity and E and k are the energy and wavenumber of the electrons. The number of electrons that play a role in the total current is equal to the number of states between the chemical potential of the contacts (Fig. 2.1.b), where each state occupies $\Delta k = 2\pi/L$. This is represented as [27]

$$N = 2\int_{k_D}^{k_S} \frac{L}{2\pi}\mathrm{d}k, \tag{2.3}$$

where the factor of 2 comes from the spin degeneracy and $k_{S,D}$ are the wavenumber of the electrons on the leads that correspond to the chemical potentials $\mu_{S,D}$. Combining Eq. 2.1 with Eq. 2.3, we obtain

$$I = e \cdot N/\tau = 2e\int_{k_D}^{k_S} \frac{L}{2\pi}\frac{1}{\tau}\mathrm{d}k = 2e\int_{k_D}^{k_S} \frac{L}{2\pi}\frac{1}{\hbar L}\frac{\mathrm{d}E}{\mathrm{d}k}\mathrm{d}k. \tag{2.4}$$

Changing the integration variable to energy, the total current takes the form:

$$I = \frac{2e}{h}\int_{\mu_D}^{\mu_S} \mathrm{d}E = \frac{2e}{h}\cdot(\mu_S - \mu_D). \tag{2.5}$$

Finally, to calculate the conductance of the quantum wire, we divide Eq. 2.5 by the applied bias $V = (\mu_S - \mu_D)/e$ to obtain its conductance:

$$G_0 = \frac{2e^2}{h}. \tag{2.6}$$

The quantity G_0 is called the *conductance quantum* and corresponds to the conductance of a perfectly conducting quantum channel. An extension of this result can be used for less ideal systems where scattering events can occur in the channel. We can model that case as a non-transparent scattering region in the quantum wire (Fig.2.1.b). Then, the conductance through the channel is related to the transmission probability $\mathcal{T}$ as

$$G = \mathcal{T} \cdot G_0. \tag{2.7}$$

As a simplified picture, in the case of an Au point-contact $\mathcal{T} = 1$, as the single-atom junction acts as an ideal quantum wire. On the other hand, in a molecular junction, the transmission probability is normally of the order of $\mathcal{T} \sim 10^{-5}$, leading to a conductance much smaller than G_0.

If we generalized for a case where multiple channels are involved in the charges transport, we can write the conductance as a sum over all the available channels where each one has a transmission probability $\mathcal{T}_n$:

$$G = G_0 \sum_{n=1} \mathcal{T}_n. \tag{2.8}$$

Following this approach we reach the so-called Landauer formula [28, 29]:

$$I(V) = \frac{G_0}{e} \int_0^\infty \mathcal{T}(E) \cdot [f(E, \mu_S) - f(E, \mu_D)] \, \mathrm{d}E, \tag{2.9}$$

where $f(E, \mu_{S,D})$ is the energy distribution of electrons on the leads that can be described with the Fermi-Dirac distribution

$$f(E, \mu) = \frac{1}{1 + \exp(\frac{E-\mu}{k_B T})}. \tag{2.10}$$

2.2 Molecular orbitals

In this section, we will apply the analysis done before for the case of a molecular junction. Let's consider a single molecule connected to two gold contacts as illustrated in the schematic of Fig. 2.2.a. To apply this formalism, we model the electrons in the molecule as an ideal Fermi gas. In a single molecule, electrons are situated in orbitals around the nuclei. These orbitals, called molecular orbitals, have discrete energy levels filled from the lowest energy to the highest energy, as presented on the left side of Fig. 2.2.b. The most important orbitals for charge transport are the lowest unoccupied orbital (LUMO) and the highest occupied orbital (HOMO) because they are the closest to the Fermi energy and thus they can contribute to the charge transport through the molecule.

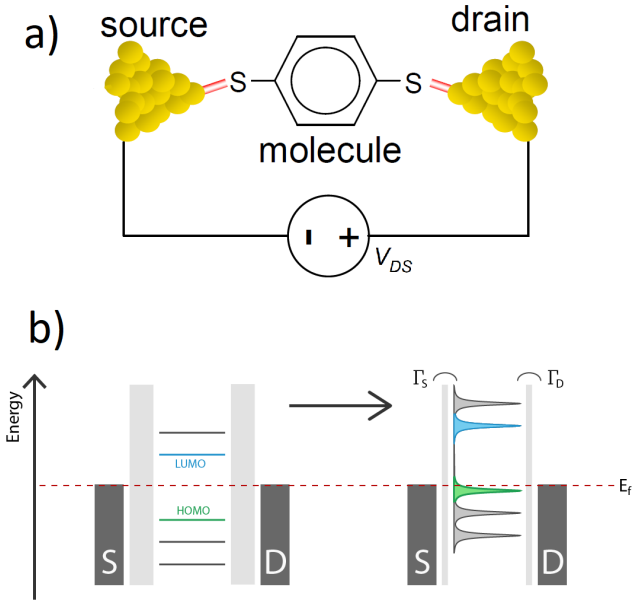

Figure 2.2: **a)** Molecular junction consisting of a single molecule attached to two gold contacts. **b)** Molecular energy levels before (left) and after (right) attaching to the contacts.

Similar to the case of a one-dimensional quantum wire, if the chemical potentials of the source and drain are the same ($\mu_S = \mu_D = E_f$), there is no current flowing through the system. To allow the current to flow, we need to apply a bias between the contacts, and a molecular energy level has to lay between the chemical potentials (the *bias window*). The transport occurs through the energy level closest to the Fermi energy. Depending on the position of the molecular orbitals with respect to the Fermi energy, this energy level can be either the HOMO or the LUMO.

If we consider a single molecule without interactions with the environment, the energy levels of the molecular orbitals can be described as a Dirac delta function. Nevertheless, when the molecule approaches a metal surface, the wave function of the molecule starts to overlap with the wave function of the metal [30]. This overlap can lead to the formation of chemical bonds between the molecule and the contacts, affecting directly the molecular orbital by *broadening* its density of states (right side of Fig. 2.2.b). This interaction between the molecule and the electrodes is represented by the *electronic coupling* $\Gamma = \Gamma_S + \Gamma_D$, where $\Gamma_{S,D}$ are the electron transfer rate at the source and drain between the molecule and the lead.

If the couplings are weak, the molecular orbitals are almost not affected by the electrodes, so we can consider them as discrete. As the interaction between the molecule and the electrodes is weak, if an electron is transported into the molecule it stays there long enough to lose the information of its phase before it is transported out of the molecule. This is called *sequential tunneling*. On the other hand, if the coupling is strong, it causes level broadening and hybridization of the molecular energy levels with the ones from the leads, where the transport is mainly *coherent tunneling*, i.e., the information on the phase is preserved. The latter is typically the case for single molecule junctions at cryogenic temperatures, whereas at room temperatures the coupling is in an intermediate regime between weak and strong.

For small molecules, the energy spacing between molecular orbitals is typically much larger than the bias window, so we can assume that only one energy level is present in the system. This model is called *single-level model*. To use this model in the analysis discussed in the previous section, we will now focus on the strong coupling regime, where the transport is mainly coherent. In this model, the transmission probability in 2.9 is written as

$$\mathcal{T}(E) = 2\pi \frac{\Gamma_S \Gamma_D}{\Gamma_S + \Gamma_D} D(E) = \frac{\Gamma_S \Gamma_D}{(E-\varepsilon)^2 + (\Gamma_S + \Gamma_D)^2/4}, \tag{2.11}$$

where $D(E)$ is the density of states. This distribution is typically modeled as a Lorentzian distribution centered around an energy ε, expressed as

$$D(E) = \frac{1}{2\pi} \frac{\Gamma_S + \Gamma_D}{(E-\varepsilon)^2 + (\Gamma_S + \Gamma_D)^2/4}. \tag{2.12}$$

Thus, the equation 2.11 can be written as

$$\mathcal{T}(E) = \frac{\Gamma_S \Gamma_D}{(E-\varepsilon)^2 + (\Gamma_S + \Gamma_D)^2/4}. \tag{2.13}$$

If we assume symmetric coupling ($\Gamma_S = \Gamma_D = \Gamma/2$) we can obtain an analytical solution for the current:

$$I(V) = \frac{G_0 \Gamma}{e} \left[\arctan\left(\frac{\varepsilon_0 + eV/2}{\Gamma} \right) - \arctan\left(\frac{\varepsilon_0 - eV/2}{\Gamma} \right) \right], \tag{2.14}$$

where $\varepsilon_0 = E_f - \varepsilon$ is the *level alignment*. The details of the description and analysis of this model can be found in Refs [31, 32]. As a brief explanation (see Fig. 2.3), the $I(V)$ curve has an S-like shape with an abrupt increase in the current when the level approaches the resonant condition $|eV/2| \to \varepsilon$. An increase of the coupling Γ leads to a less abrupt shape and also to a high saturated current, changing the level alignment ε shifts the resonance position, and larger $|\varepsilon|$ moves apart from the positive and negative resonance. The transmission gap between these two positions delimits the off-resonant transport regime.

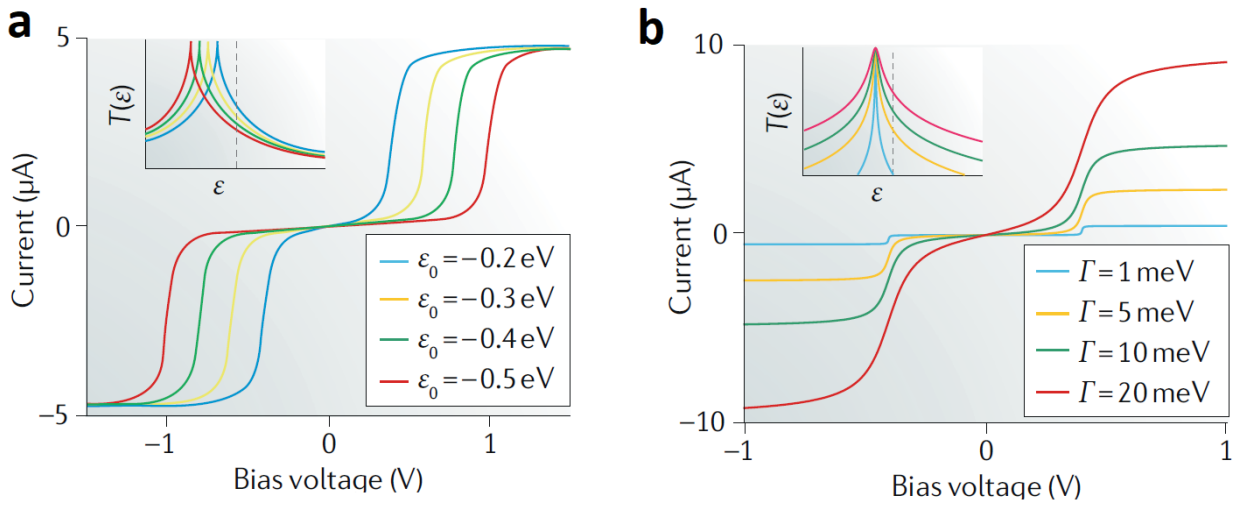

Figure 2.3: Figure extracted from Ref. [32]. a) Shape of I-V curve for $\Gamma = 20$ meV for different energy positions of the single level. Bringing the single level closer to E_f results in a higher zero-bias conductance. b) By reducing the total electronic coupling The constant current level at high bias is reduced and the step in current becomes narrower.

This model is frequently used in the literature to fit experimental data. With this curve shape, it is possible to extract the level alignment ε and the broadening Γ of the molecular junction. Nevertheless, the extracted parameters have to be carefully interpreted as this curve is only suitable for the case of a single-level model in the strong coupling regime at low bias, where off-resonant coherent transport takes place and fails to fit the experimental results at high bias.

2.3 Tunneling current

To understand what happens in the case where no molecule is bridging the gap between both contacts, we can model this gap as a rectangular barrier $U(x)$ with a potential energy of ϕ

and a length d. Thus, the energy landscape is given by

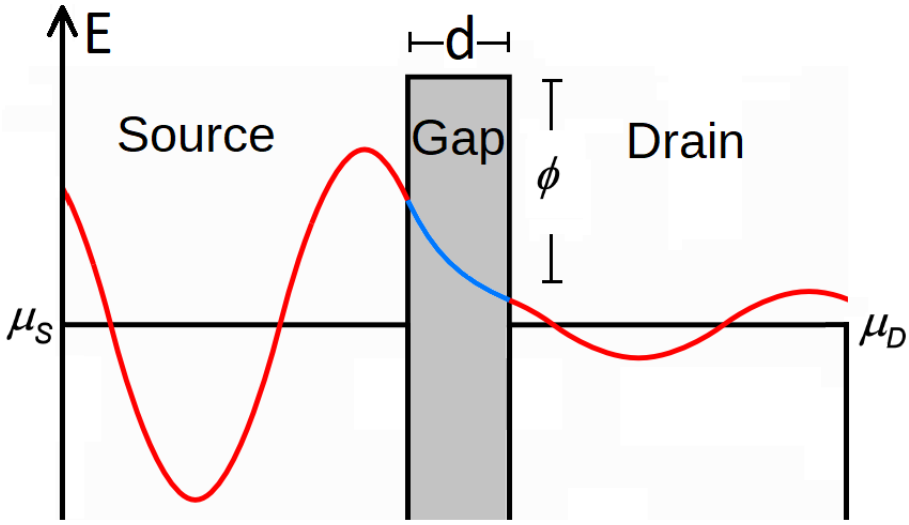

Figure 2.4: Schematic illustration of the energy landscape in the case of tunneling. The barrier has a height ϕ and a width d. The red line represents the electron wave-function.

$$U(x)\begin{cases}\phi & x \in [0,\mathrm{d}] \\ 0 & x \notin [0,\mathrm{d}].\end{cases} \tag{2.15}$$

To obtain the transmission probability of this system, we will consider the electrons as traveling planar waves coming from the source electrode. Then, the wave-function of the electrons can be expressed by the time-independent Schrödinger equation:

$$-\frac{\hbar^2}{2m}\frac{\mathrm{d}\psi(x)}{\mathrm{d}x} + U(x)\psi(x) = E\psi(x), \tag{2.16}$$

where E is the energy of the electron. We can obtain the solution of the Schrödinger equation for each region independently

$$\psi(x)\begin{cases}C_1 \cdot e^{\mathrm{i}kx} + C_2 \cdot e^{-\mathrm{i}kx} & x < 0 \\ C_3 \cdot e^{\mathrm{i}k'x} + C_4 \cdot e^{-\mathrm{i}k'x} & 0 \le x \le \mathrm{d} \\ C_5 \cdot e^{\mathrm{i}kx} & x > \mathrm{d},\end{cases} \tag{2.17}$$

where

$$k = \sqrt{\frac{2m(\phi - E)}{\hbar^2}}, \quad k' = \sqrt{\frac{2m(E)}{\hbar^2}}. \tag{2.18}$$

Notice that the exponential along with the constants C_1 and C_5 correspond to the incident and transmitted wave, respectively. Thus, we can obtain the transmission probability $\mathcal{T}(E)$ as $\mathcal{T}(E) = (C_5/C_1)^2$. If we apply the boundary conditions that ψ and $\mathrm{d}\psi/\mathrm{d}x$ are continuous in the two intersections of our model, we can obtain the transmission probability as

$$\mathcal{T}(E) = \left(\frac{C_5}{C_1}\right)^2 = exp(-2d\sqrt{2m_e(\phi - E)}/\hbar). \tag{2.19}$$

Finally, if we use Eq. 2.19 and Eq. 2.1, we can obtain the so-called Simmons equation for the current density [33]:

$$I = \frac{eA}{2\pi h d^2} \cdot \left(\phi e^{-2d\sqrt{2m_e\phi}/\hbar} - (\phi + eV)e^{-2d\sqrt{2m_e(\phi+eV)}/\hbar}\right), \tag{2.20}$$

where V is the bias voltage and A the electrode area. Figure 2.5 shows the characteristic IV curve calculated with the Simmons equation for different barrier height. As can be seen, the shape of these curves is similar to the ones from figure 2.3 near-zero bias voltage. However, these curves are smooth and do not have a saturation level.

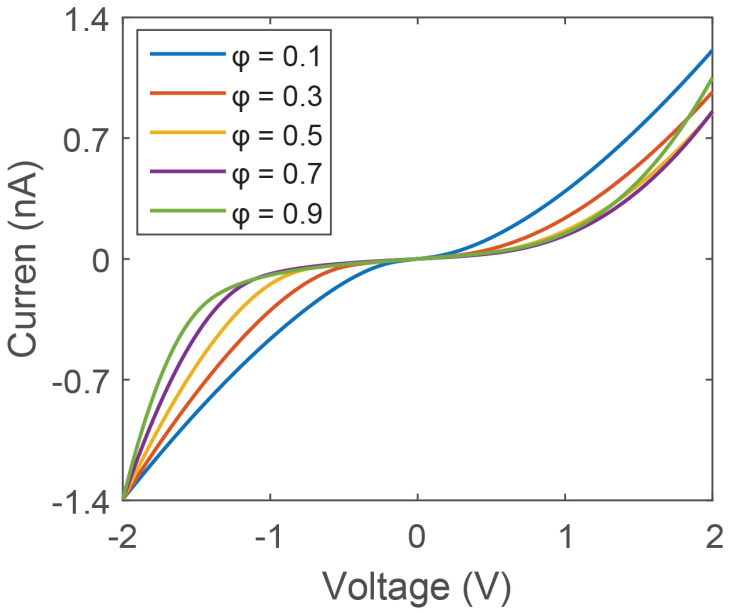

Figure 2.5: Current trough a tunnel junction, simulated by using the Simmons model (programmed in Matlab, extracted from Ref. [34]), where ϕ varies between 0.1 and 0.9.

Chapter 3

Methodology

All the measurements carried out for this thesis were done using the mechanically controllable break-junction (MCBJ) technique. The mechanism of this technique works as follows: a thin gold wire is deposited on top of a flexible substrate. The constriction is 100 nm wide and is suspended after etching the sample with oxygen plasma. This substrate is clamped on both sides to a three-point bending mechanism, shown in Fig. 3.1. The substrate is then bent by a pushing rod stretching the gold wire until it breaks. Thus, both ends of the broken wire act as electrodes. The gold wire can be fused again moving the pushing rod back, allowing to break and make the junction thousands of times without noticeable deterioration of the wire. Because of the geometry of the sample, the vertical movement of the pushing rod is related to the horizontal movement of the electrodes with a ratio of the order of $1 : 10^{-5}$, allowing sub-nanometer control over the separation of the electrodes.

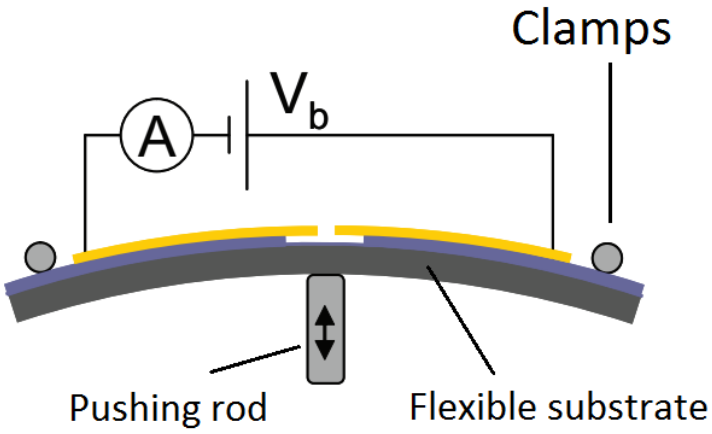

Figure 3.1: Schematic of the architecture of the MCBJ technique.

3.1 Experimental set-up

A detailed description of the MCBJ set-up can be found in [9, 30, 35, 36]. Here, only a brief explanation of the important features will be presented. The diagram of the set-up is illustrated in Fig. 3.2. The set-up description can be separated into mechanics, electronics and programming parts.

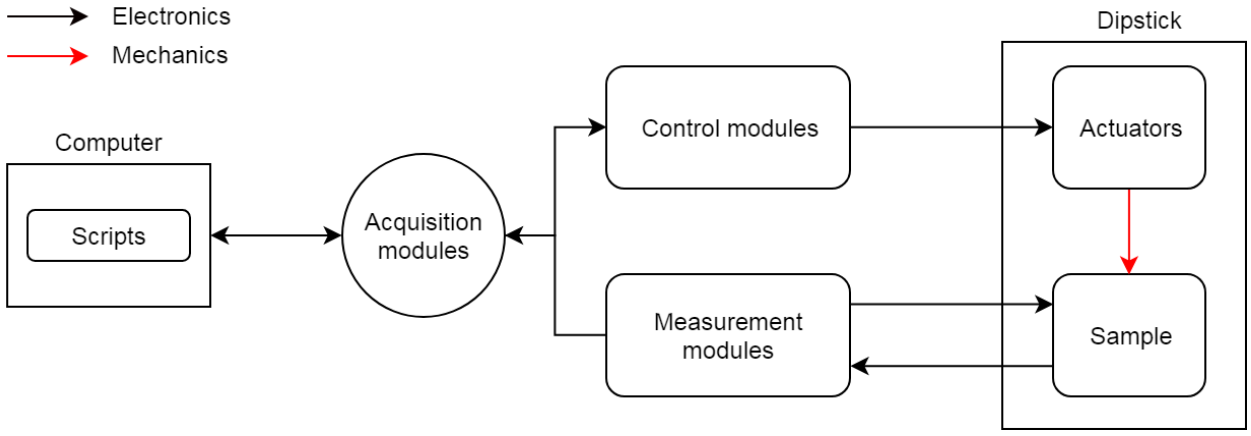

Figure 3.2: Diagram of the MCBJ set-up used. The description can be separated between mechanics (right), electronics (center) and programming (left).

3.1.1 Mechanics

The sample is positioned in a three-points bending mechanism (Fig. 3.3.a) and can be deformed in two ways: moving the pushing rod up or moving the sample down. The former is done by a piezoelectric element positioned at the back of the bending mechanism. This element pushes a cantilever connected to the pushing rod, as shown in Fig. 3.3.b. For the experiments, a commercial piezoelectric element from *Physik Instrumente* is used, which has a maximum speed of 800 μm/s with a step of 150 μm. This element is responsive and fast, but with a limited displacement range. The latter is done by controlling the clamps, which are connected by a differential screw to a driving axis, controlled by a servo motor positioned on top of the set-up (See Fig. 3.3.c). A brushless servo motor from *Faulhaber* is used. The motor has a maximum speed of 5 μm/s with a minimum step of 0.1 μm. This element has a large dynamic range but it is relatively slow in comparison with the piezoelectric element.

The function of the motor is to bring the substrate to a bending close to the rupture point of the gold wire since it has a large dynamic range. The motor increases the tension slowly and when the junction is broken, the motor stops and the piezoelectric element is used to move the electrodes just before breaking. Then, the piezoelectric element breaks and makes the junction at a higher speed while the conductance is been measured. This type of measurement is called *fast-breaking* measurement.

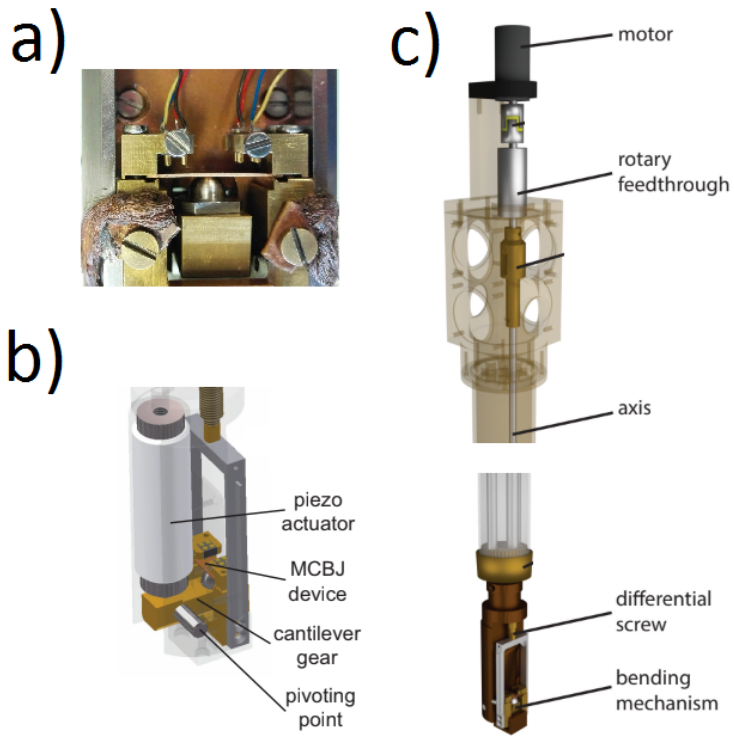

Figure 3.3: MCBJ set-up schematic. a) Three-point bending mechanism with a sample inside; b) piezoelectric element; c) motor actuator (top) connected to the bending mechanism (bottom). Some figures were extracted from [9].

3.1.2 Electronics

The electronics can be subdivided in control and measurement electronics. The control electronics are composed of the piezo controller and the motor driver. The piezo controller is connected to an *ADwin Gold* unit which is operated by the computer. The motor driver, on the other hand, is connected directly to the computer.

The measurement electronics components were developed by Raymond Schouten (TU Delft). These are hosted in a shielded rack (IVVI rack) powered by two batteries to avoid the noise coming from the power line. A fixed bias voltage is applied to the junctions and the current is measured to obtain the conductance. The current is measured with a transimpedance logarithmic amplifier, with a precision of $\approx$ 10 pA and a dynamic range of about ten orders of magnitude. This wide range allows us to measure the conductance of a gold junction ($\sim 1\ G_0$) and a molecular junction ($\sim 10^{-5}\ G_0$) without need to change amplifier. The analog signal from the IVVI rack is converted to a digital signal by the ADwin Gold and then sent to the computer.

3.1.3 Programming

The experimental set-up is almost completely controlled by computer. Homemade Python scripts are used to control and measure both the motor and the ADwin. This, in turn, controls the piezoelectric element and measure the analog signal. To interact with the ADwin Gold, a homemade library in ADbasic is used.

3.2 Measurement procedure

The samples are bent thousands of times to break and make the junction. During this process, the conductance is constantly being measured. A *conductance trace* consist of the measured conductance G as a function of the electrode displacement d. In the case of a clean junction (*i.e.* before molecule deposition) the conductance of the wire before breaking decreases with the displacement as its cross-section decreases. The conductance continues to decrease until the junction is a single atom wide. In this case, the conductance is equal to the conductance quantum 1 G_0. Further bending results in the breaking of the junction. Because of the tension before breaking the electrodes snap-backs, making a gap between them so the conductance drops drastically. The current that can still be measured is now caused by the tunneling effect between the electrodes, which decays exponentially as a function of displacement (Fig. 3.4 in purple).

If a molecule is around the junction at the breaking point, it can bridge the gap between the electrodes when the junction is broken. The conductance is now through the molecule and a step or *plateau* is present in the conductance trace as the conductance remains roughly constant, until the connection is lost and the conductance drop to the noise level (Fig. 3.4 in red).

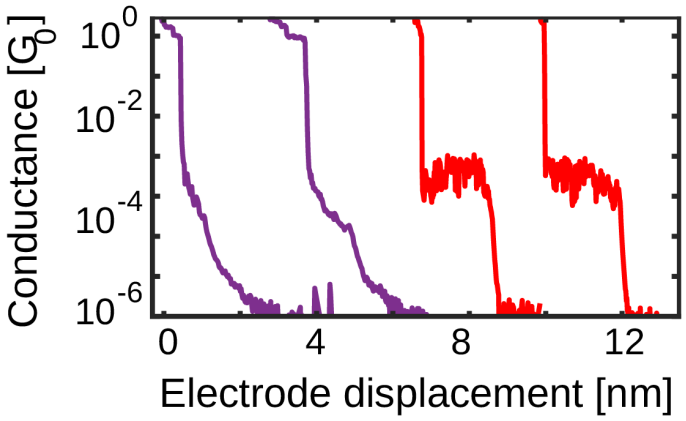

Figure 3.4: Semi-logarithmic plot of individual conductance traces for the case of with (red) and without (purple) a molecular junction. The traces are horizontally displaced for clarity.

To measure single molecules in dry conditions, the molecule is prepared in a solution with a concentration of 0.1 mM. Then, a small amount of the solution is dropcasted at the

center of the sample. After the solvent is completely evaporated the measurement starts. As a general rule, the bare gold (before dropcasting molecules) is always measured before the molecular measurements with the same parameters in order to have a control measurement. Thus, only samples with *clean* control measurements are used.

3.2.1 Histogram generation

We measure the conductance versus the displacement of the junctions. As the geometry and the dynamic of the junction cannot be controlled at the sub-nanometer scale, especially at room temperature, measuring only one conductance trace is not enough to draw conclusions about the conductance value. Therefore, we measure thousands of traces and we look for the most common and reproducible behaviors. To picture these behaviors, all the traces are merged into a two-dimensional (2D) histogram, where the diagram is divided into *bins* and the color scale reflects the number of counts on each bin. Then, if multiple traces follow the same behavior, a clear pattern is present in the 2D histogram (see Fig. 3.5.a).

Another useful representation of the data is the one-dimensional (1D) histogram, where only the conductance distribution is presented. In this case, each bin represents the number of counts with similar conductance, independent of the displacement. This can be seen as the sum of each row of the 2D histogram (Fig. 3.5.b). As the range of conductance is 7-8 orders of magnitude wide, all the histograms in this thesis, both one and two dimensional, have a logarithmic scale in the conductance axis.

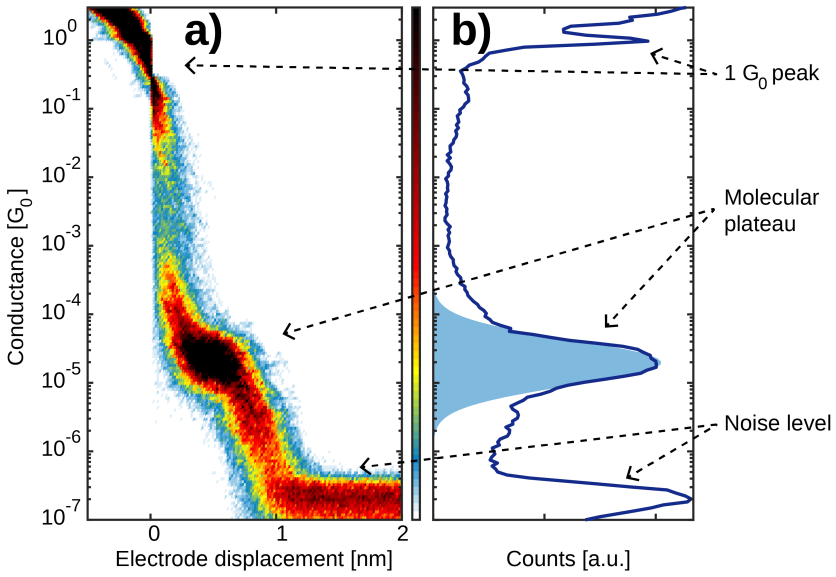

Figure 3.5: a) 2D histogram and b) 1D histogram of an example measurements. In the image the 1 G_0, molecular plateau and noise level are indicated.

3.2.2 Distance calibration

The relation between the vertical displacement of the pushing rod and the horizontal displacement of the electrodes is called *attenuation factor*. As the junction structure can change between samples because of small differences in the fabrication process or positioning of the sample, the attenuation factor is not a fixed value between different samples. Two methods can be used to obtain this value: the length of the 1 G_0 plateau and the steepness of the tunneling slope (Fig. 3.6).

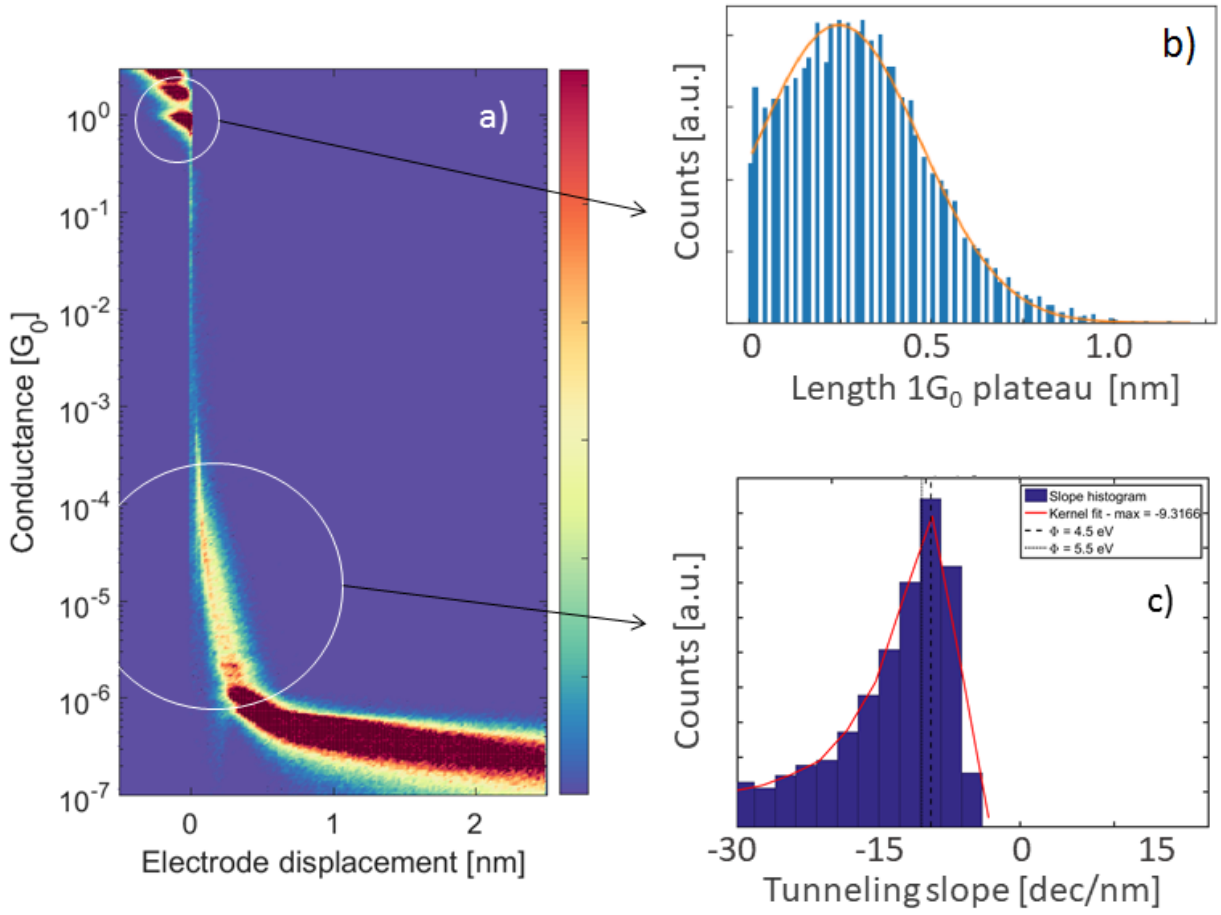

Figure 3.6: a) 2D histogram of a bare gold measurement. b) histogram of the length of the 1 G_0 plateau. c) Slop histogram of the tunneling decay, where the vertical dashed lines represent the theoretical values for different work functions.

The 1 G_0 plateau comes from the single Au atom junction prior to the breaking event. The inter-atomic distance of this chain has been shown to be 0.25 nm [37]. Thus, the attenuation factor can be chosen so the median value of the 1 G_0 plateau is similar to the expected value (Fig. 3.6.b).

The second method to calibrate the distance is to use the bare gold measurements to obtain the tunneling slope. To do this, we can use the Simmon's equation (Eq. 2.20) from the last chapter. For the case where $eV \ll \phi$; the current has an exponential relation with

the displacement [38]:

$$I(d) \propto \exp(-2d\sqrt{2m_{\mathrm{e}}\phi}/\hbar). \tag{3.1}$$

In a logaritmic scale, we can obtain the theoretical tunneling slope if we consider the gold work function to be ~ 5 eV (Fig. 3.6.c):

$$-\frac{2d}{\hbar}\sqrt{2m_{\mathrm{e}}\phi} \approx -10 \text{ dec/nm}. \tag{3.2}$$

Each method has its benefits and drawbacks. The first method is considered the most effective one, but not all the breaking events present a well defined 1 G_0 plateau and the length histogram is not easy to fit. While the second method shows good results for cryogenic temperatures, at room temperatures it is experimentally found that the gold work function can change depending on the environmental conditions, affecting drastically the expected slope. Using both methods, together with having control measurements, can assure an acceptable calibration. Nevertheless, claims based on plateau length in molecular measurements should be treated carefully.

Chapter 4

Data analysis

Break-junctions measurements are intrinsically stochastic. Therefore, they require the acquisition of large data sets to gain insight into the electronic properties of the molecule under study. Hence, there is a need to develop statistical tools for the analysis of the measured data, in order to capture the complexity of the molecular junction. To achieve this, the first step is to separate the interesting events (molecular traces) from the uninteresting ones (tunneling traces). This is not an easy task as the percentage of molecular traces is generally low and their breaking behavior is *a priori* unknown.

Different techniques have been used to filter the data in the past with different benefits and drawbacks [39, 40]. But conventional analysis has a strong focus on the most prominent class of signals and smaller groups in the data may remain unnoticed. To overcome the current limitations, many efforts have been made to introduce machine learning in the data selection, using techniques like vector-based analysis [41], density peaks clustering [42] or hierarchical data structure [43].

Machine learning provides a great advantage, as it allows us to select the data in a methodical and unbiased way. Machine learning tools can be subdivided into two main groups: supervised and unsupervised learning. Supervised algorithms are based on the fact that the result is known, so the algorithm can be trained with data already processed until the output is equal to the expected result. An example of supervised learning is the artificial neural networks used in image recognition to identify, for example, dogs an cats. As the result can be found easily by the user, the neural network is trained with selected images where the *labels* "cat" or "dog" are known until the algorithm can predict the labels of new images with low error rate.

In contrast, unsupervised learning is implemented when the result is unknown or when less human intervention is needed. This type of algorithm is used to detect underlying structures of the data that otherwise is not clear how to distinguish. An example of this is the customer segmentation of a brand or shop, where the purchasing history and customer behavior can be used to identify associated patterns.

In this thesis, the unsupervised K-Means clustering algorithm was used to filter the mea-

sured data, following the procedure of [44], which will be explained in this chapter. First, a general qualitative explanation of the K-Means algorithm will be given, followed by how the data is represented in order to use this algorithm. Then, the general procedure and the limitations of this technique are presented.

4.1 K-means algorithm

The K-means algorithm is a very popular clustering algorithm due to its conceptual simplicity, low computational cost and scalability [45]. K-means is a classification algorithm that seeks to split the data in a given number of *clusters* or *classes*.

To explain the algorithm, let us consider a dataset where 2 variables are collected [46]. The data points can then be presented in a 2D plot where each axis represents one variable, as in Fig. 4.1, left. This is called the *feature space*. Then, we want to split the data into 4 different clusters. In K-means, the first step is to initialize the centers or *centroids* of the clusters at random positions. Then, a first classification is made: Every point will be assigned to the centroid that is closer to it. We will call this step the *E-Step*. The next step is to evaluate the new center of the cluster. The new position is calculated as the average position of all the points that belong to that cluster. We will call this the *M-Step*. With the new position, some points are now closer to a different centroid and will be assigned to that cluster instead. Thus, the E-Step and M-Step are repeated until the new position of the M-Step is the same as the old position, and the final clusters are selected.

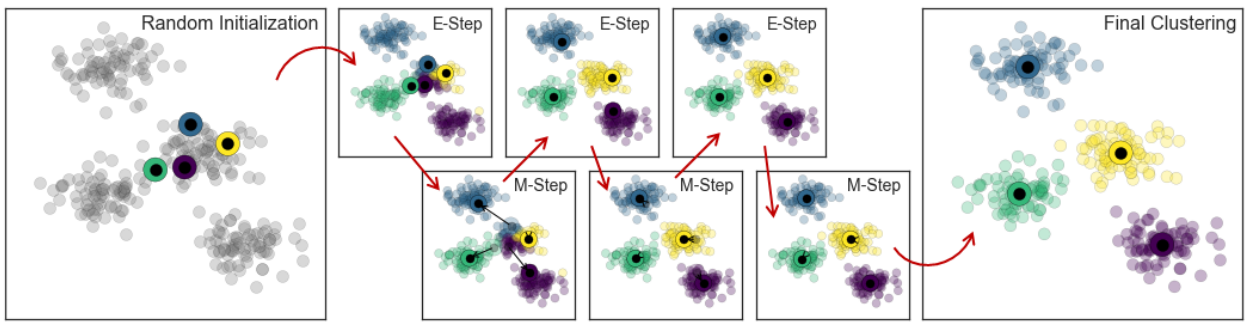

Figure 4.1: Step-by-step evolution of the K-means algorithm (from left to right). For the description of each step, see the main text. Figure extracted from Ref. [47]

Depending on the input data, the final results can vary from one initialization to another. Therefore, to optimize the classification task, the K-means algorithm is run multiple times with different initial parameters. The final classification result is the one corresponding to the smallest cost function, defined as the sum of the squared distances from each point to its centroid.

4.2 Feature space and data representation

The feature space used in this thesis is described in [44]. The creation of this feature space is partly inspired by the well-known MNIST dataset for handwritten digits, where the images of the digits are reduced to a 28×28 pixel images [48]. In the present case, each breaking trace is converted into a 2D histogram image with a resolution of M×N bins, where M and N are chosen by the user, as it is shown in Fig. 4.2. Then, every image is converted from a matrix to a vector. This vector is called *feature vector* and corresponds to the position of each trace in a new space called *feature space*, where each bin of the feature vector represents one dimension in the feature space, and the value of that bin is the coordinate value of the trace in that dimension (similar as in 4.1). As the histograms have M×N bins, the clustering algorithm has to deal with a high-dimensional feature space.

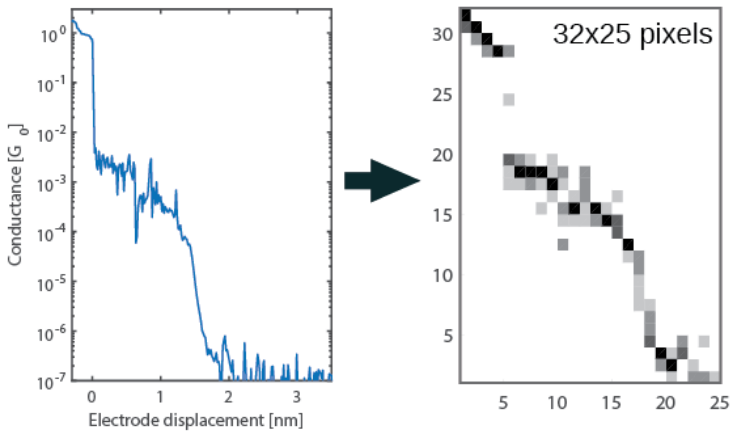

Figure 4.2: Feature space generation. Each conductance trace (left) is converted to a 2D histogram (right) with M×N pixels or bins. Each bin represent a dimension of the feature space and the number of counts of them is the coordinate value on that dimension.

To gain more insight into the molecular junction, each conductance can be also represented in a 1D conductance histogram with L number of bins. This can be added to the feature space as extra dimensions, leading to a feature space with M×N+L dimensions. Notice that even though the clustering method works in a high-dimensional space, the final clusters are then converted back to 2D and 1D histograms showed previously in order to illustrate the analyzed data in the same way as the raw data. As an example, in Fig. 4.3 the raw data of a molecular measurement is presented along with three different classes after using the clustering method explained here.

4.3 General procedure and limitations

In the case of MCBJ measurements, the first and most important step is to be able to split empty traces (traces only with exponential decay attributed to tunneling) and molecular

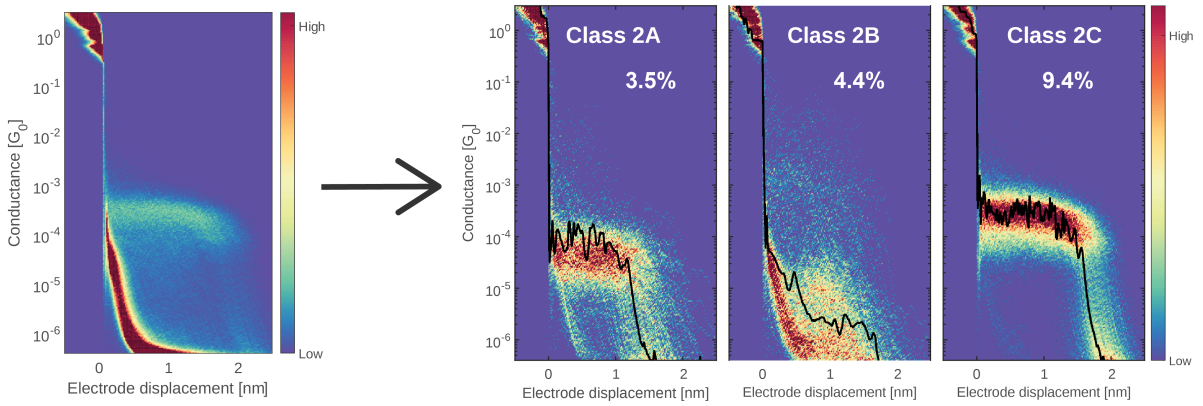

Figure 4.3: Example of the results using the clustering method explained in this chapter. On the left, the raw data of a porphyrin-based molecule is presented, while on the right, three classes obtained after clustering are shown. Notice that the empty class is not presented (See section 4.3).

traces (traces with plateau-like features or peaks in the 1D histogram). For that purpose, the following procedure is used to choose the number of clusters:

1. Each conductance trace is converted to a 2D semi-logarithmic histogram with 32x20 bins and a 100-bins 1D logarithmic histogram (see section 4.2). The resolution of the 2D histograms is chosen to be 4 bins per decade (vertical axis) and 1 bin per angstrom (horizontal axis).
2. The K-means algorithm is used with 100 different initialization (see section 4.1). As a first step, a low number of clusters is used, normally 2-3 clusters.
3. If the result is not satisfactory, the algorithm is run again. The number of classes is increased until the empty traces can be visually separated from the molecular traces.
4. Then, the K-means algorithm is used only in the empty cluster to create sub-clusters and thus be sure there is no molecular signature inside it.
5. If needed, sub-clusters can be created in the molecular clusters to split different configurations.
6. Finally, similar classes are merged to present the final result. As a general rule, two clusters can be merged if they present a similar breaking pattern and the 1D histogram of the merged data shows a single peak.

4.3.1 Limitations

To understand the limitations of the classification procedure, we have to understand which are the assumptions behind it. K-means algorithm has three implicit assumptions [49]:

- All the variables have the same variance,
- Clusters are spatially distributed, *i.e.*, the distribution of each variable is spherical,
- Each cluster has almost the same number of observations.

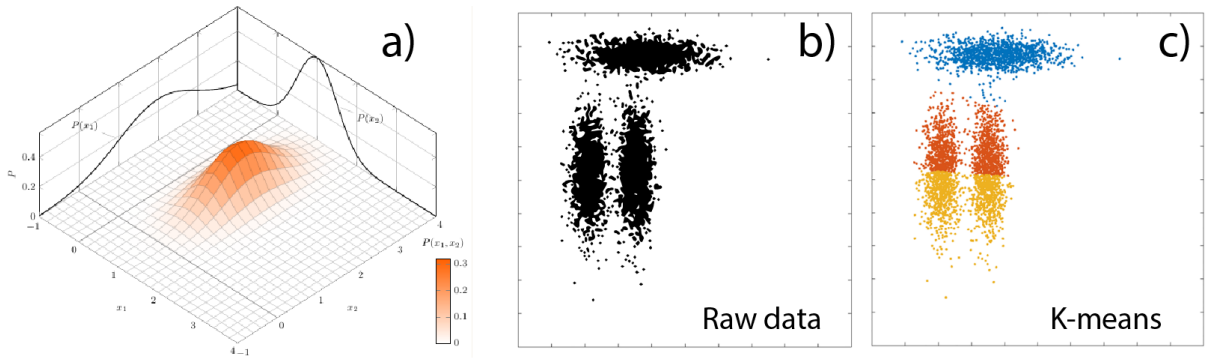

Figure 4.4: a) Example of a 2 dimensional set of data where each variable has different variance. b) example data and c) after using K-Means, where it fails to separate the 3 classes. Figure extracted from Ref. [50]

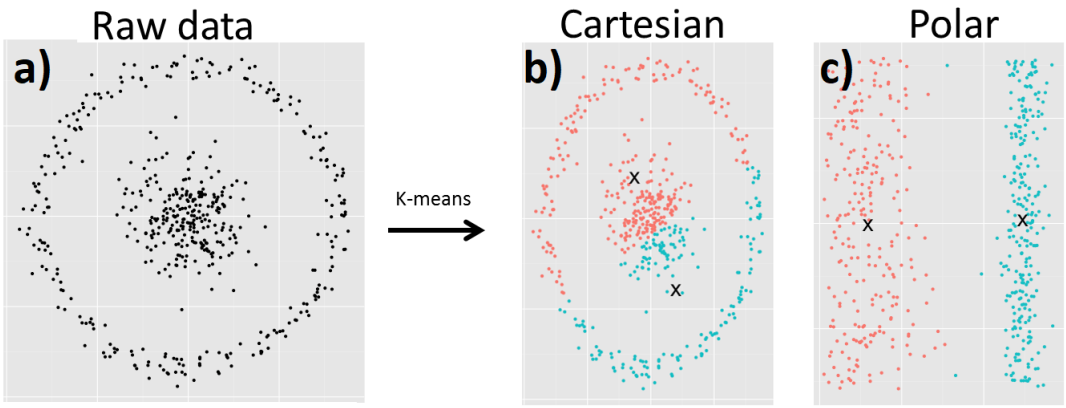

Figure 4.5: a) example data where the second assumption is not fulfilled. b) results after using K-Means with 2 clusters are shown. K-means fails to cluster the two rings in a Cartesian representation. c) changing to polar coordinates the algorithm works correctly. Ref. [49]

Figure 4.6: Example where the third assumption is not fulfilled. At the left, the raw data is presented and, at the right, the results after using K-Means with 2 clusters are shown. K-means fails to separate the small group with the rest of points. Ref. [51]

If any of the assumptions are not met, the algorithm will "fail" in classifying the data, *i.e.* the clusters cannot be found in a single run. Although the first and second assumptions can be met changing the way of representing the data (see Fig 4.5), the third assumption depends strongly on the measurements and cannot be controlled. Even more, the high dimensional feature space in our procedure makes it difficult, to see if the first 2 assumptions are really fulfilled. However, even if the algorithm "fails", the method can still be used to analyze the data if clusters are merged and sub-clusters are made, although the result, in that case, depends on the procedure used.

Finally, it is important to stress that every conductance trace measured is different, so general conclusions about the properties of a molecule must arise from a statistical analysis of the whole data set and not from an individual or few traces. Thus, the number of clusters cannot be separated from the experimental resolution nor the physical interpretation.

Chapter 5

Conductance measurement of porphyrin molecules

The results presented in the following chapters were published and can be found in Ref. [52]. All the molecules measured for this thesis were synthesized by Patrick Zwick from the Mayor group at the University of Basel.

Porphyrins are attractive to study as they are present in a variety of biological processes in nature. In particular, they are interesting for molecular electronics as they are stable, easy to synthesize and have low attenuation β factor (see Section 1). In this project, we studied the influence of structural features of porphyrin-based compounds using the MCBJ technique for transport measurements. For this reason, we synthesized seven different compounds with similar geometry, changing the bulkiness of the substituents and adding or removing anchoring groups and metal ions in the center of the structure.

The chemical structure of each measured porphyrin can be found in Fig 5.1. Every molecule was methodically and purposefully synthesize in order to study the influence of every module in the conductance of the molecule. Compound **P1**, **P2** and **P3** share the same linear backbone, consisting of the porphyrin core, phenylene-acetylene spacers and thiol anchoring groups, but vary in their lateral bulky groups. These measurements are used to study the influence of the bulky groups. On the other hand, **ZnP1**, a variant of **P1** which includes a Zn(II) ion in the center of the molecule, is employed to investigate if the presence of a metal center affects the conductance of the porphyrin.

R1, **R2** and **R3** are based in the compound **P1** as they possess the same lateral bulky groups and are used to investigate the role of the anchoring groups and the spacers. **R1** has the same structure as **P1**, but only one side exposes the anchoring groups with the spacer, while at another side both groups are replaced with a bulky group. Similarly, in **R2** both sides were replaced with bulky groups, leading to a molecule with bulky groups only. And finally, **R3** has a similar backbone as **P1** but here only the anchoring group is replaced with the bulky group, without taking off the spacers.

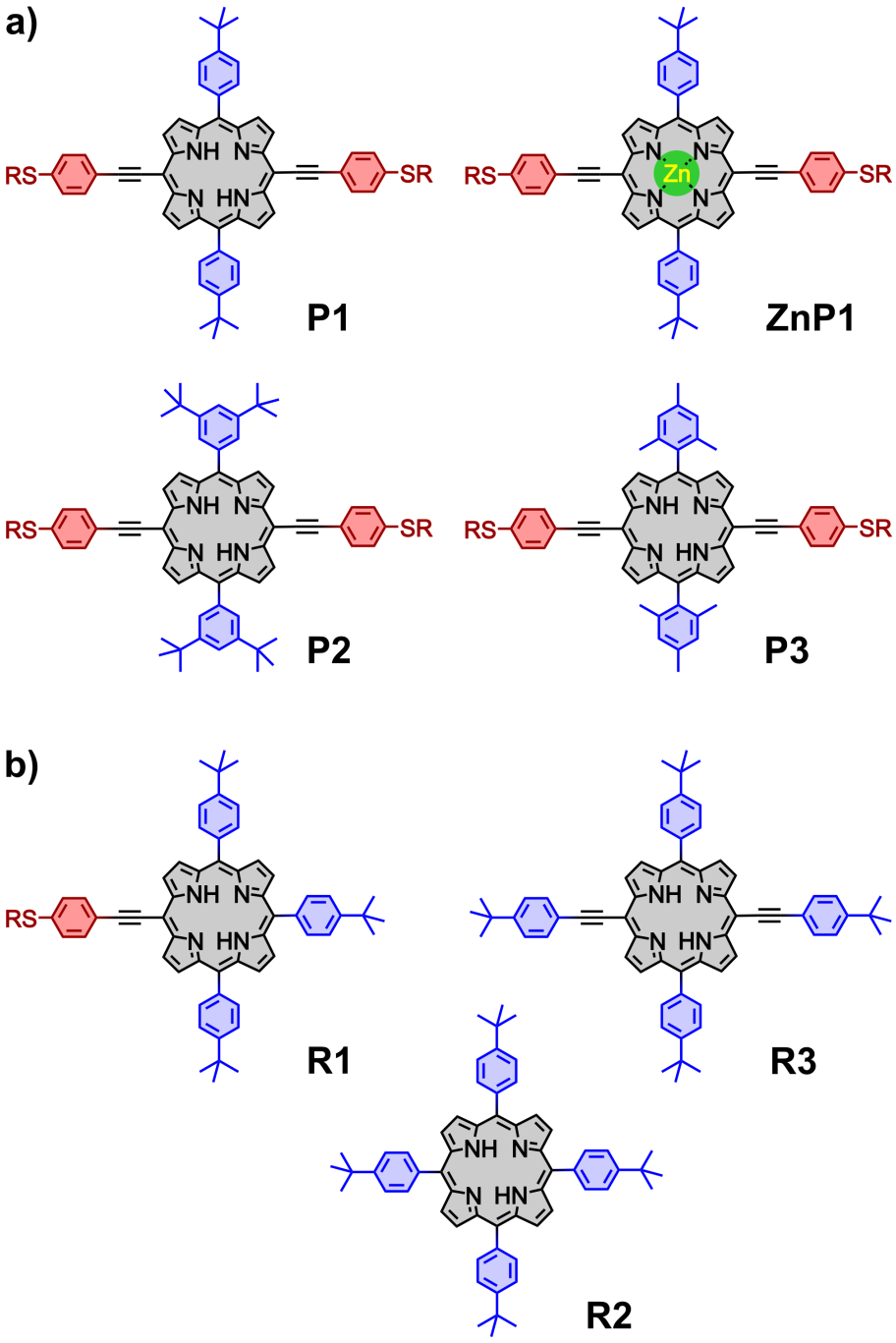

Figure 5.1: a) Structural designs of **P1**, **ZnP1**, **P2** and **P3**; b) structural formula of **R1**, **R2** and **R3**. The different parts of the molecule have been coloured dividing the anchoring groups (red) and the bulky side groups (blue). The molecules are synthesized with R=acetyl, but upon deprotection at the electrode surface, R represents either a hydrogen atom or the gold electrode.

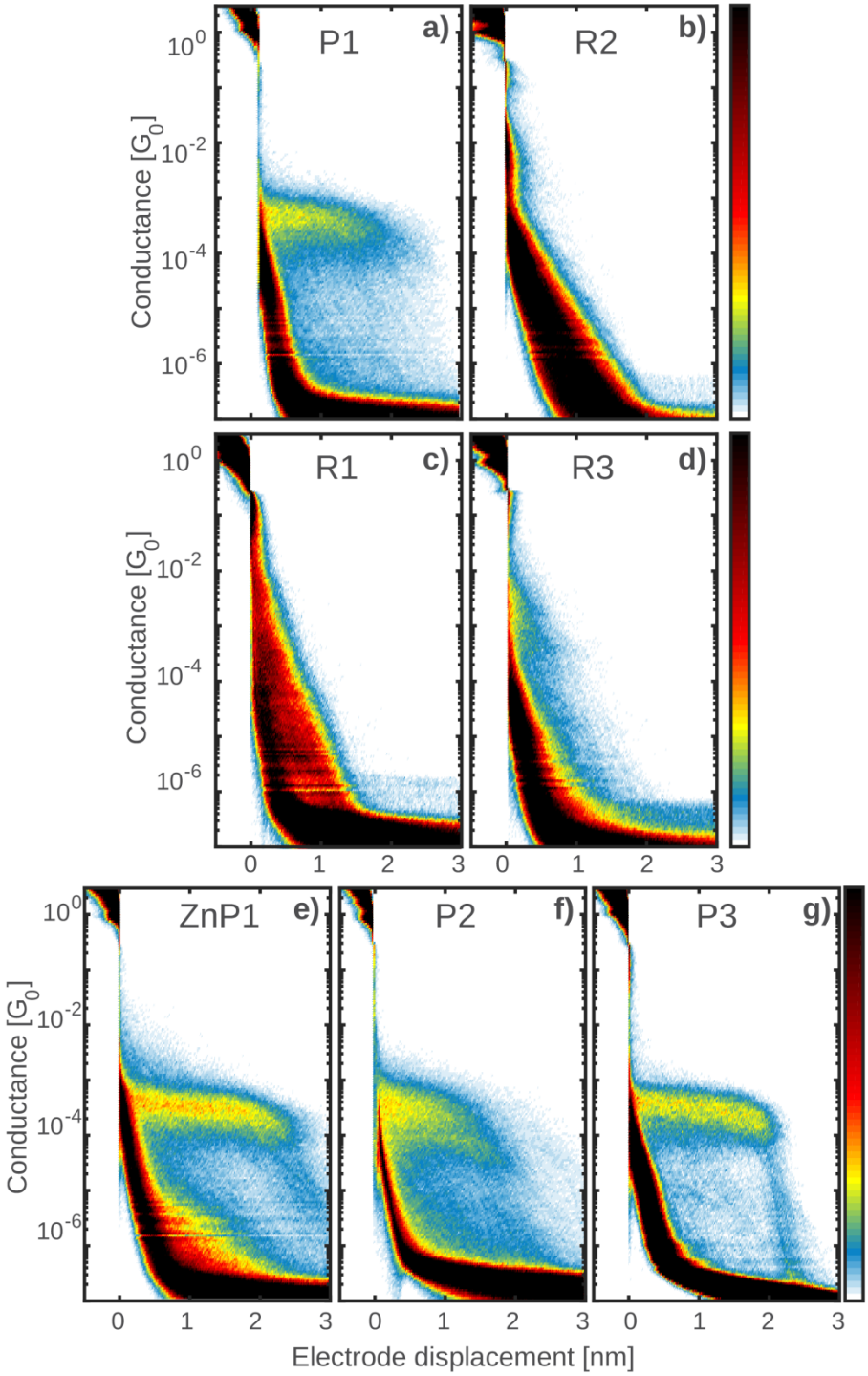

Figure 5.2: a)-g) Two-dimensional (2D) conductance versus displacement histograms built from 10 000 consecutive breaking traces of P1, R1, R2, R3, ZnP1, P2 and P3. no data selection was made. All measurements were performed with a bias of 100 mV and a bending speed of 6 μm/s at room temperature. The insets represent the chemical structure of each measurement.

For each molecule, 10 000 consecutive traces were recorded without data selection. The bias voltage used for all the measurements was 100 mV. Fig. 5.2 shows the 2D histograms of every molecule.

As can be seen from Fig. 5.2, **P1**, **P2**, **P3** and **ZnP1** show a very well defined plateau with a conductance value above $1 \times 10^{-4} G_0$ longer than 2 nm, whereas **R1**, **R2** and **R3** do not show this clear feature. To illustrate this difference, examples of individual breaking traces recorded for **P1** and **R2** are presented in Fig. 5.3.

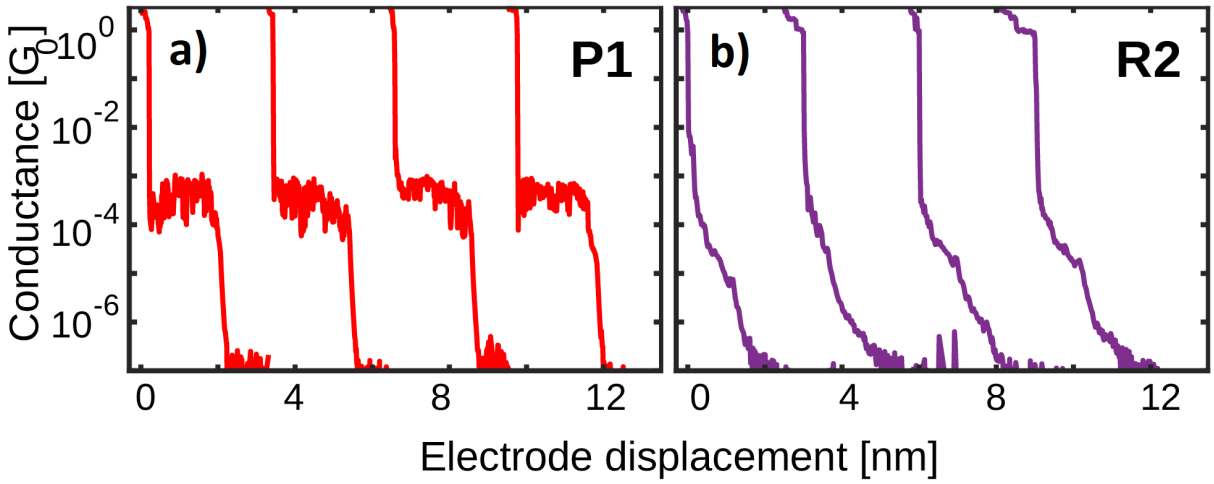

Figure 5.3: Examples of individual conductance breaking traces for a) **P1** and b) **R2** (with a horizontal offset of 3 nm for clarity).

To get more insight into the electronic properties of the porphyrins, we employed the unsupervised clustering algorithm mentioned in section 4.1. Using the raw data of the seven different molecules, we identify classes of common behaviors in the breaking traces and their correlation with structural features of the molecules, intending to link each of them to a different electron pathway across the porphyrins. In figure 5.4 three of the four classes from **P1** are shown. Class A-C are associated with the presence of a molecule inside the junction, while Class D (the excluded one) contains the traces in which no molecular junction has been formed and only shows the exponential decay typical of tunneling through a barrier. More information can be found in the Appendix.

In this case, Class A constitutes 64.7% of the molecular junctions and contains the traces that exhibit a plateau of about 2.2 nm length. A log-normal fit to the peak in the 1D conductance histogram reveals it being centered around $2 \times 10^{-4} G_0$. The traces grouped in Class B (28.8%) form a slightly shorter and wider plateau, centered at $3 \times 10^{-5} G_0$. Finally, Class C (6.5%) shows a broad feature centered at $2 \times 10^{-6} G_0$. The three classes together constitute 12.6% of the total traces.

To investigate the stability of the molecule in the junction and to get more information about the different classes, *self-breaking* measurement was also performed for the case of the compound **P1**.

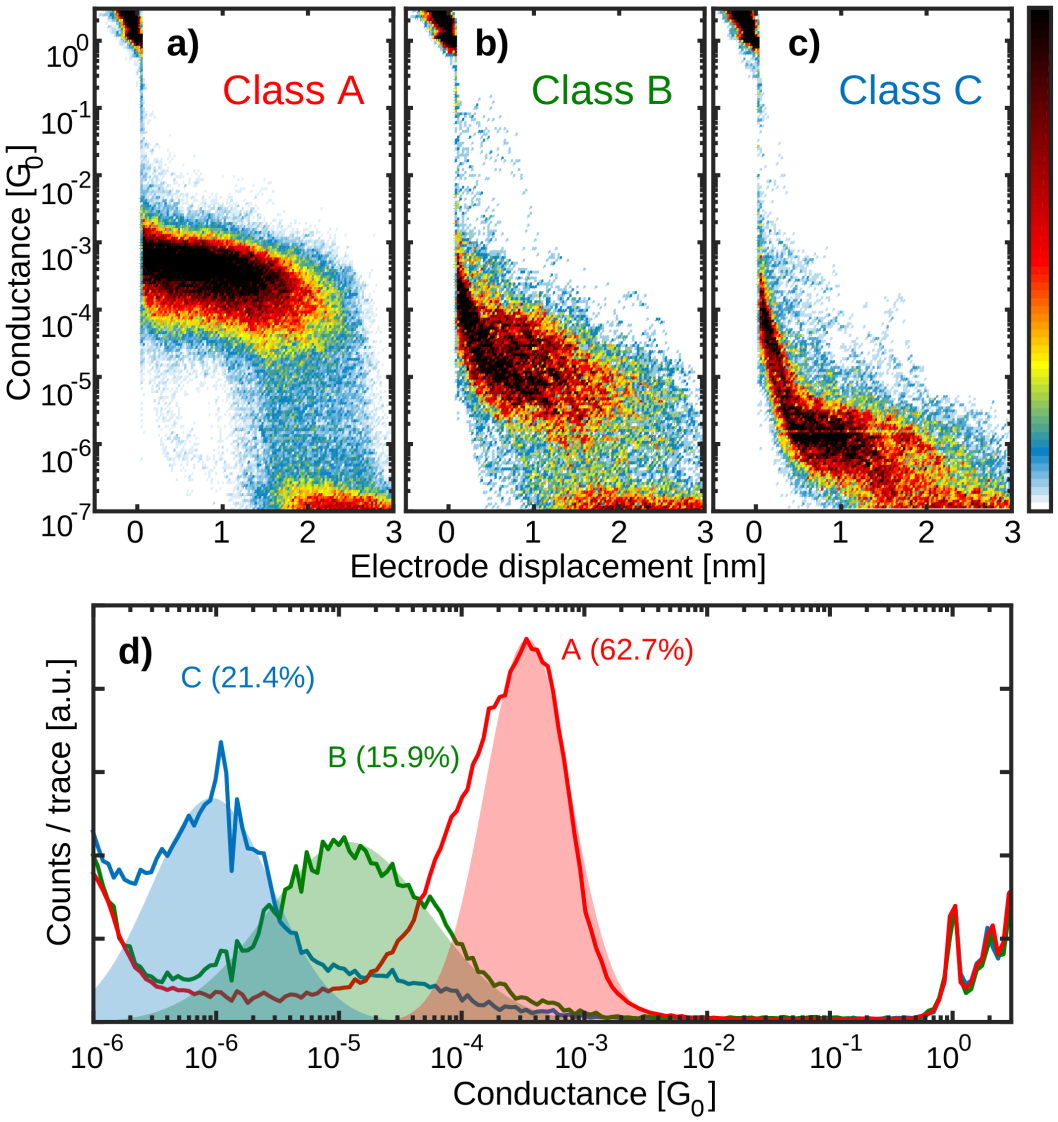

Figure 5.4: Clustering analysis of the conductance properties of **P1**. a-c) Two-dimensional histograms of the three different categories of breaking traces obtained from the reference-free cluster analysis applied to **P1**. d) One-dimensional conductance histograms corresponding to Class A, B and C. By fitting a log-normal distribution to the one-dimensional histograms, we can extract the conductance peak positions at $2 \times 10^{-4} G_0$ for Class A (64.7% of the molecular traces), $3 \times 10^{-5} G_0$ for Class B (28.8%) and $2 \times 10^{-6} G_0$ in the case of Class C (6.5%).

5.1 Self-breaking measurements

Unlike *fast-breaking* measurements, in *self-breaking* the piezo element is not used to open and close the junction. In these measurements, the piezo element bends the sample until the conductance is close to 1 G_0, just before breaking. Then, the piezo stops and it waits for the junction to break by itself because of the tension in the constriction. If no molecule is around the junction, the conductance drops to the noise level and the junction is merged again for a new measurement. But if a molecule is attached to the gold electrodes, the junction will stay

open and recording the conductance as long as the molecule can be attached. Thus, if the molecule can form a stable molecular junction, it can be attached for longer periods. This kind of measurements allow us to probe the lifetime of the junction, which is a consequence of the strength of the binding, and the conductance value of the molecule in a configuration that does not necessarily coincide with those obtained in fast-breaking measurements.

In figure 5.5 the self-breaking measurements of **P1** are presented. The plateaus between 3×10^{-5} and $1 \times 10^{-3} G_0$ are the most stable ones, with a junction lifetime up to 5 minutes. The longest self-breaking traces can be mostly associated with the Class A from the fast breaking. Note that the peak around $3 \times 10^{-5} G_0$ present in the 1D histograms is attributed to long traces (up to 300 seconds, the time limit of the measurements) corresponding to Class A.

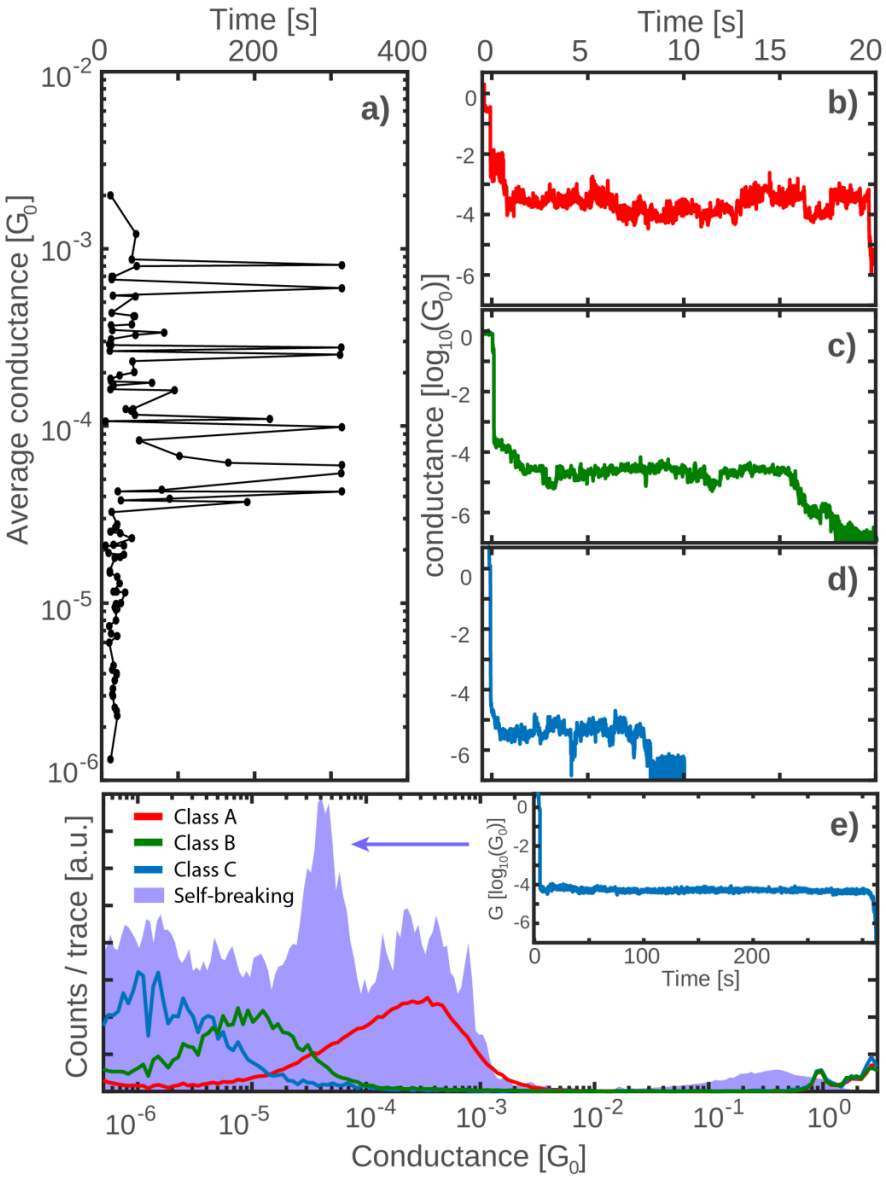

Figure 5.5: Self-breaking measurements for P1. a) Average conductance vs time of 384 self-breaking traces. The maximum recorded time was 300 seconds. b)-c) Examples of single traces corresponding to Class A (red), Class B (green) and Class C (blue). e) 1D histogram of self-breaking traces (purple area) and fast-breaking traces for each class (solid lines).

Chapter 6

Analysis and discussion

In this chapter, the data from every molecule will be compared to identifying the different electronic pathways inside the porphyrin. Using the clustering analysis we found four different classes (class A, B, C and the excluded traces). In table 6.1 the presence of each class in every molecule is shown. Comparing the occurrence of each class for the various molecules we can relate them with a specific charge path. In order to do so, the result of every molecule for each class will be compared separately in the following sections.

Molecule	Class A	Class B	Class C
P1	✓	✓	✓
P2	✓	✓	✓
P3	✓	✓	✓
ZnP1	✓	✓	✓
R1			✓
R2			
R3		✓	✓

Table 6.1: Summary of the occurrence of the three molecular classes for each molecule. Class A corresponds to the high-conductance class, class B to the medium-conductance class and class C corresponds to the low-conductance class.

6.1 Class A

Class A corresponds to the high-conductance plateau and is present in all the four main molecules: **P1**, **P2**, **P3** and **ZnP1**. The 2D histograms are shown in figure 6.1. Although there are some differences in the *shape* of the plateau, the *conductance value* of all the four molecules is around the same value and the observed differences in plateau conductance or length are within the variations typically found in MCBJ experiments even when performed on the same molecule [53].

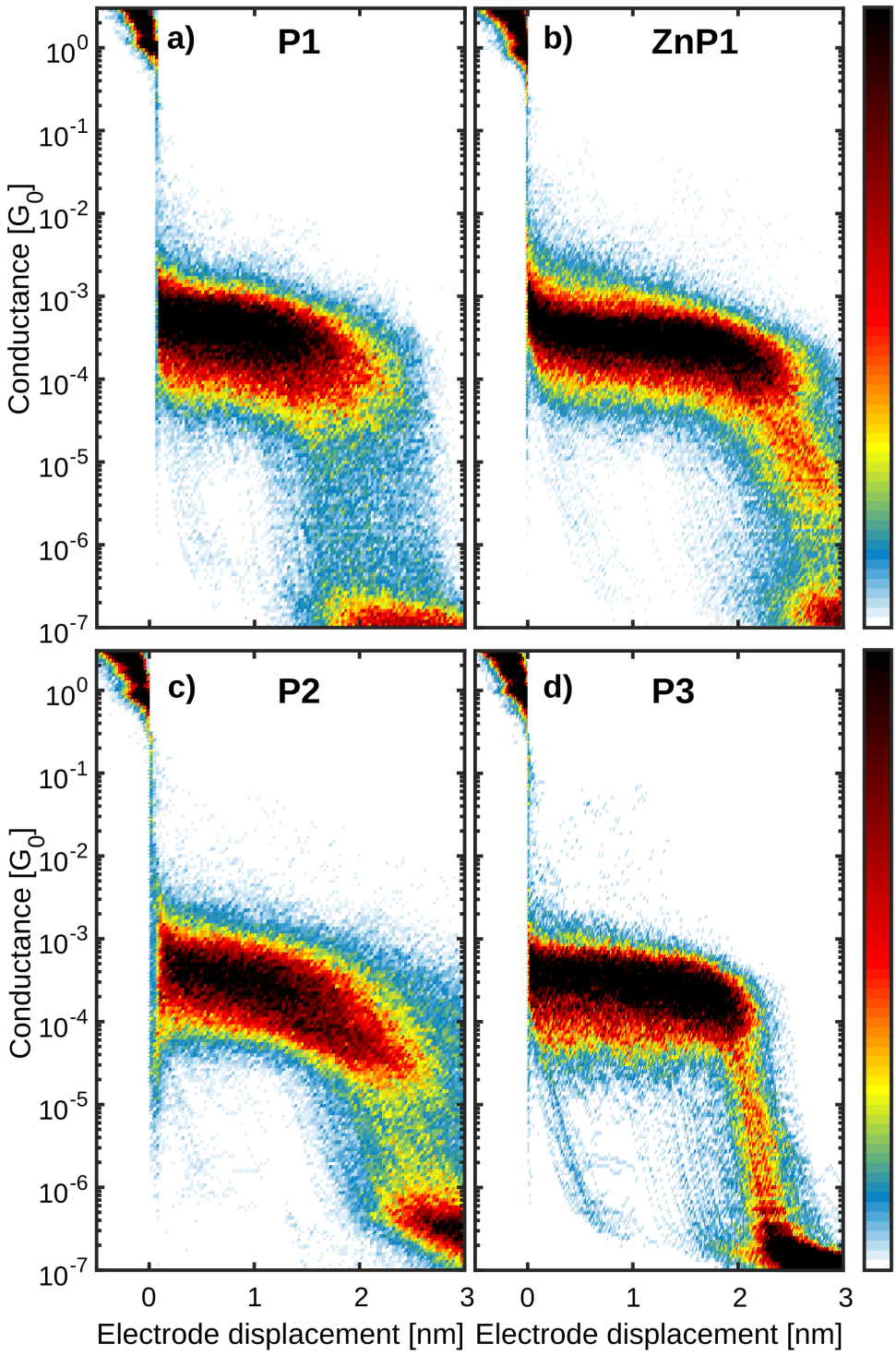

Figure 6.1: Two-dimensional conductance vs. displacement histograms for a) **P1**, b) **ZnP1**, c) **P2** and d) **P3**. The histograms only include breaking traces with the behaviour present in class A. All datasets have similar length and conductance values.

We attribute this feature to the junction configuration in which the molecule is connected to both electrodes via the anchoring groups and transport occurs from sulfur to sulfur. This is supported by the average trace length of about 2 nm, which is in good agreement with the estimated length from the crystallographic measurements of the fully stretched molecule

length (Fig.6.2).

Noticeably, the presence of the Zn atom does not affect this plateau, indicating that the electron paths involved in transport are mainly localized around the core of the porphyrin and not inside it [54]. We further note that for **P3**, class A exhibits the least slanted conductance plateau with the narrowest distribution (see Table S1). Besides, the breaking of the molecular junction around 2 nm occurs in a more defined way compared to the other derivatives. In this respect, it is interesting that the bulky groups of **P3** are more spatially localized above and below the porphyrin system than for the other molecules **P1** and **P2**, thus reducing access to the π system of the porphyrin core.

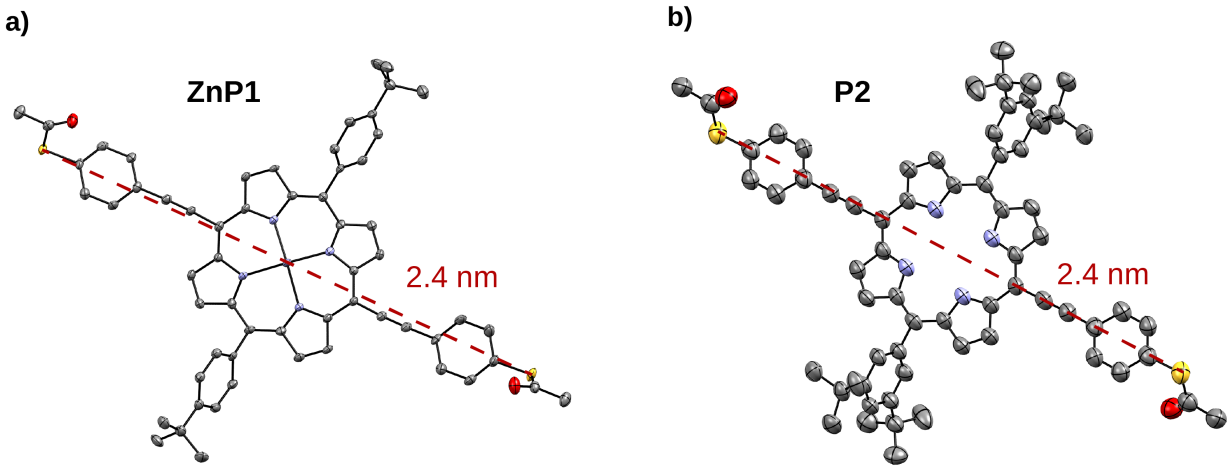

Figure 6.2: Representation of the solid state structures of a) **P2** and b) **ZnP1**. The dashed red line displays the main axis and the S-S distance.

6.2 Class B

In figure 6.3 class B from molecules **P1** and **R3** are shown for comparison. As it is shown in table 6.1, this class is present in all the four main molecules **P1**, **P2**, **P3** and **ZnP1**, and in the reference molecule **R3**; while is not observed for the porhpyrin compounds without both spacer groups (**R1** and **R2**). This suggests that their presence introduces another transport pathways.

Compared to that observed in class A, the plateau in class B has a lower conductance, is shorter, more spread out and observed less frequently. In the case of **R3**, not containing any anchoring group, this plateau is more slanted than **P1**. Hence, the presence of these anchoring groups seems to stabilize the junction, yielding more defined plateaus *even if the electron injection does not occur through the sulfur atom*. The charge transport pathway could thus involve the spacer group or the porphine ring at both sides of the molecule, as it is not observed in molecules that do not contain these groups.

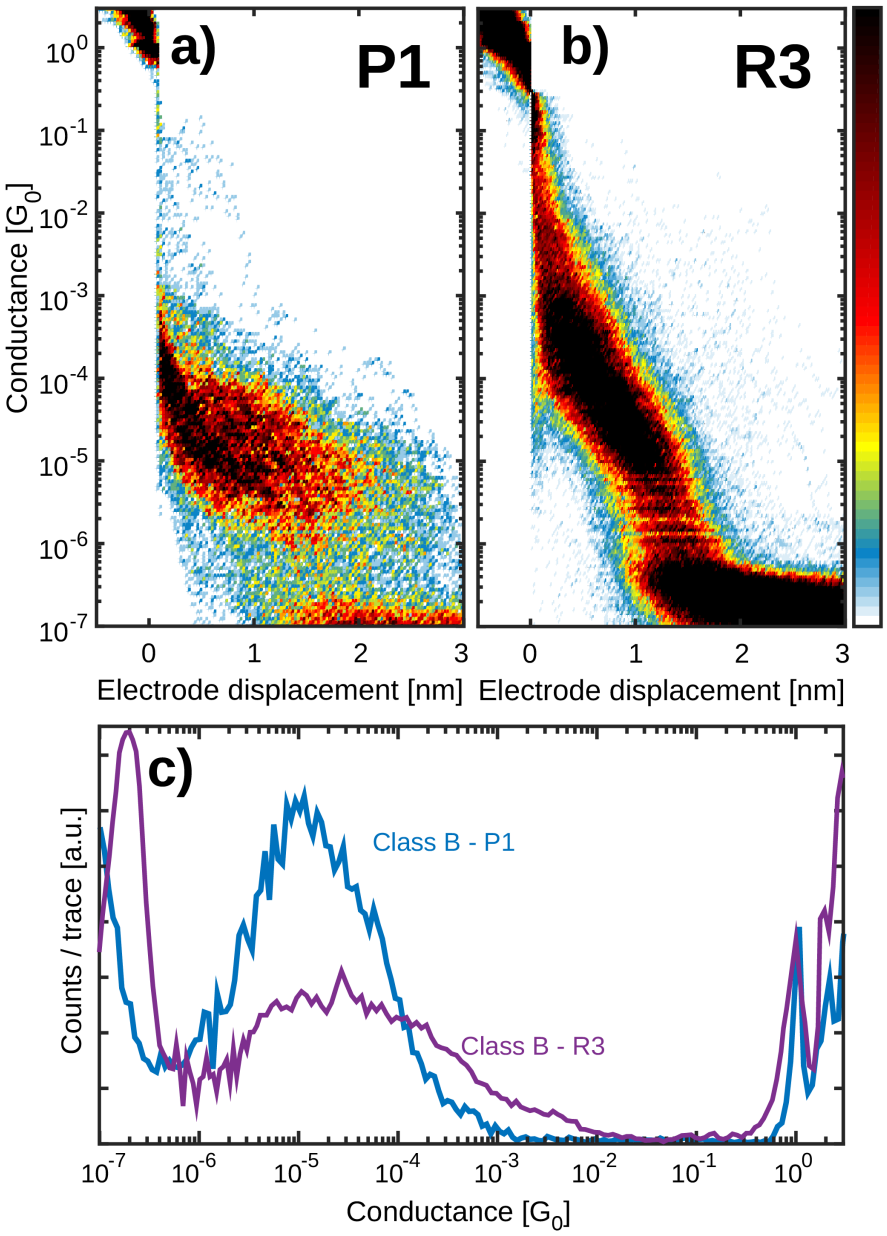

Figure 6.3: Two-dimensional histograms of Class B from molecules a) P1 and b) R3. d) 1D conductance histogram for Class B from P1 (blue) and R3 (purple).

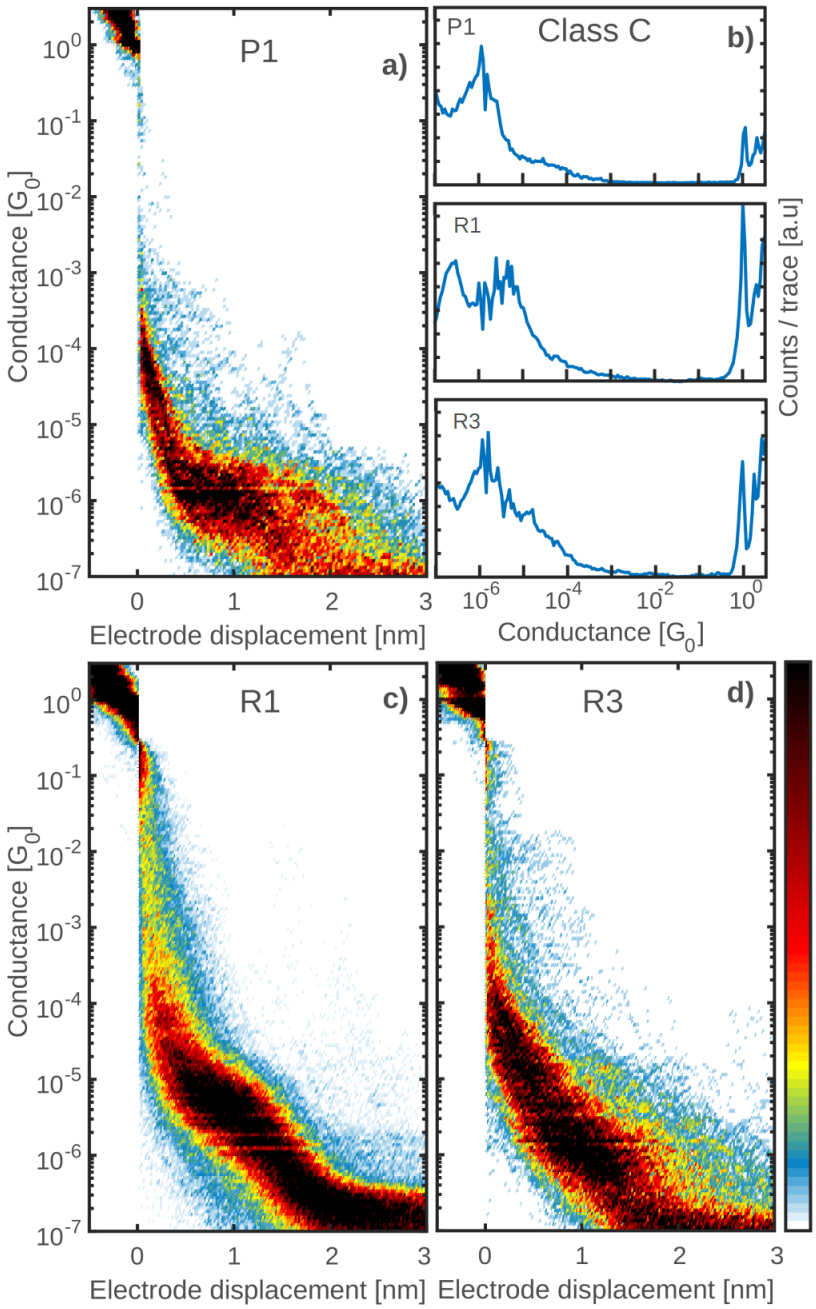

Figure 6.4: a) 2D conductance versus displacement histograms of class C from **P1**. b) 1D conductance histograms of class C from **P1** and from two control measurements (**R1 and R3**). c), d) 2D histograms of classes from **R1** and **R3**, respectively

6.3 Class C

Class C corresponds to the low-conductance class and is present in all the measured molecules except **R2**, which do not have any spacer or anchoring group. In figure 6.4 the 2D and 1D

histograms of class C are shown for the case of **P1**, **R1** and **R3**.

Class C can be related to the path that results from injection in the π-system of the spacer group and ends at one of the lateral bulky group. Nevertheless, the bulky group should not play a role in the conductance of the molecule because it cannot attach to the gold electrodes. Thus, this interaction is not a binding connection but a tunneling current mediated by the bulky group. This interpretation is validated as the conductance range of this class is very low, similar to the tunneling current between the gold electrodes in an empty junction.

As can be seen in Fig. 6.4, the plateau from **R3** is more slanted, again suggesting that the sulfur plays a role in the stability of the junction configuration. The role of the sulfur in mechanically stabilizing the junction configuration is also corroborated by the reduced conductance spread in **R1**, which does expose one anchoring group as a potential mechanical grip, compared to **R2** and **R3**, which do not. Still, the Sulfur in the anchoring group cannot be excluded as a possible injection point in **P1** and **R1** for this class, although it does not change significantly the conductance value with respect to **R3**.

6.4 Stability and self breaking

To check the stability of the different classes, self-breaking measurements were performed in the case of compound **P1** (Fig. 5.5). While class A showed high stability (up to 5 minutes at room temperature), the lifetime of class B and C did not exceed the tens of seconds. These observations confirm the hypothesis about the mechanical stabilization role of the anchoring groups. Furthermore, the stability of the fully stretched molecule is relatively high and in the range of other well-known molecules as OPE3 [55].

Finally, it is interesting to see that the most stable configuration has a slightly lower conductance than the most probable conductance of Class A in the fast breaking measurements (Fig. 5.5.e). Suggesting that, inside the same conductance pathway, the most probable conductance is not necessarily the same as the most stable one. For this, more experiments and analysis are needed.

Conclusions

In this thesis single porphyrin-based molecule were electrically characterized using the mechanically controllable break-junction (MCBJ) technique. Seven different molecules were measured with similar yet different molecular structures, methodically and purposefully modifying their design in order to understand the conduction path inside every single molecule measured. For each molecule, at least 10 000 breaking traces were measured, constituting an unprecendently large dataset. We identified transport pathways by applying an unbiased clustering algorithm for the analysis of these breaking traces (Fig. 6.5). This clustering algorithm is based on the K-means algorithm with a high dimensional feature space specifically tailored for our experimental data.

By introducing phenylene-acetylene as spacer and thiols as anchor groups, we achieved very stable molecular junctions with a high conductance up to 2×10^{-4} G_0. Both, bulky groups and Zn ion as a metal center did not have a significant influence on the junction properties, suggesting the conductance through the molecule is mainly localized on the conjugated porphyrin system.

The observed high-conductance plateau (named *Class A*) is related to the thiol-to-thiol conduction path. Other classes with lower conductance were found and were related to the presence of phenylene-acetylene spacers. In particular, the middle conductance plateau (named *Class B*) is attributed to the acetylene-acetylene conduction path and the third slanted plateau (*Class C*) is related to a conduction path between the spacer group and one of the bulky group, *i.e.*, the acetylene-benzene conduction path.

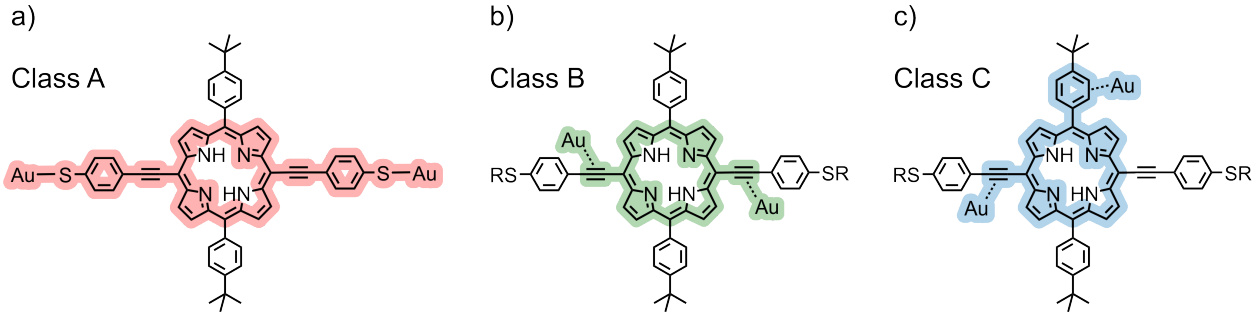

Figure 6.5: Transport pathways corresponding to the 3 different classes through the molecular structure displayed with **P1**.

Bibliography

[1] Bernhard Mann and Hans Kuhn. Tunneling through fatty acid salt monolayers. *Journal of Applied Physics*, 42(11):4398–4405, 1971.

[2] Arieh Aviram and Mark A. Ratner. Molecular rectifiers. *Chemical Physics Letters*, 29(2):277 – 283, 1974.

[3] James K. Gimzewski and Christian Joachim. Nanoscale science of single molecules using local probes. *Science*, 283(5408):1683–1688, 1999.

[4] M. A. Reed, C. Zhou, C. J. Muller, T. P. Burgin, and J. M. Tour. Conductance of a molecular junction. *Science*, 278(5336):252–254, 1997.

[5] Diana Dulić, S. J. van der Molen, T. Kudernac, H. T. Jonkman, J. J. D. de Jong, T. N. Bowden, J. van Esch, B. L. Feringa, and B. J. van Wees. One-way optoelectronic switching of photochromic molecules on gold. *Phys. Rev. Lett.*, 91:207402, Nov 2003.

[6] Yueqi Li, Marius Buerkle, Guangfeng Li, Ali Rostamian, Hui Wang, Zixiao Wang, David R. Bowler, Tsuyoshi Miyazaki, Limin Xiang, Yoshihiro Asai, Gang Zhou, and Nongjian Tao. Gate controlling of quantum interference and direct observation of anti-resonances in single molecule charge transport. *Nature Materials*, 18(4):357–363, 2019.

[7] Daniel Gerster, Joachim Reichert, Hai Bi, Johannes V. Barth, Simone M. Kaniber, Alexander W. Holleitner, Iris Visoly-Fisher, Shlomi Sergani, and Itai Carmeli. Photocurrent of a single photosynthetic protein. *Nature Nanotechnology*, 7:673, Sep 2012.

[8] Paven Thomas Mathew and Fengzhou Fang. Advances in molecular electronics: A brief review. *Engineering*, 4(6):760 – 771, 2018.

[9] M.L. Perrin. *Charge Transport Through Single-Molecule Junctions: Experiments and Theory*. TUDelft, Applied Sciences, QN/Quantum Nanoscience, 2015. `https://doi.org/10.4233/uuid:ac21689b-5818-4440-acda-00fec12be722`.

[10] M. Shakiba, J. Chen, and G. Zheng. 24 - porphyrin nanoparticles in photomedicine. In Michael R. Hamblin and Pinar Avci, editors, *Applications of Nanoscience in Photomedicine*, pages 511 – 526. Chandos Publishing, Oxford, 2015.

[11] Thijs Stuyver, Mickael Perrin, Paul Geerlings, Frank De Proft, and Mercedes Alonso. Conductance switching in expanded porphyrins through aromaticity and topology

changes. *Journal of the American Chemical Society*, 140(4):1313–1326, 2018. PMID: 29291371.

[12] Dae Hwan Yoon, Sun Bae Lee, K.-H. Yoo, Jinhee Kim, Jong Kuk Lim, Naoki Aratani, Akihiko Tsuda, Atsuhiro Osuka, and Dongho Kim. Electrical conduction through linear porphyrin arrays. *Journal of the American Chemical Society*, 125(36):11062–11064, 2003. PMID: 12952488.

[13] Bong Keun Kang, Naoki Aratani, Jong Kuk Lim, Dongho Kim, Atsuhiro Osuka, and Kyung-Hwa Yoo. Length and temperature dependence of electrical conduction through dithiolated porphyrin arrays. *Chemical Physics Letters*, 412(4):303 – 306, 2005.

[14] Gita Sedghi, Katsutoshi Sawada, Louisa J. Esdaile, Markus Hoffmann, Harry L. Anderson, Donald Bethell, Wolfgang Haiss, Simon J. Higgins, and Richard J. Nichols. Single molecule conductance of porphyrin wires with ultralow attenuation. *Journal of the American Chemical Society*, 130(27):8582–8583, 2008. PMID: 18557617.

[15] Gita Sedghi, Víctor M. García-Suárez, Louisa J. Esdaile, Harry L. Anderson, Colin J. Lambert, Santiago Martín, Donald Bethell, Simon J. Higgins, Martin Elliott, Neil Bennett, J. Emyr Macdonald, and Richard J. Nichols. Long-range electron tunnelling in oligo-porphyrin molecular wires. *Nature Nanotechnology*, 6:517 EP, Jul 2011. Article.

[16] Zhihai Li, Tae-Hong Park, Jeff Rawson, Michael J. Therien, and Eric Borguet. Quasi-ohmic single molecule charge transport through highly conjugated meso-to-meso ethyne-bridged porphyrin wires. *Nano Letters*, 12(6):2722–2727, 2012. PMID: 22500812.

[17] Gita Sedghi, Louisa J. Esdaile, Harry L. Anderson, Santiago Martin, Donald Bethell, Simon J. Higgins, and Richard J. Nichols. Comparison of the conductance of three types of porphyrin-based molecular wires: beta,meso,beta-fused tapes, meso-butadiyne-linked and twisted meso-meso linked oligomers. *Advanced Materials*, 24(5):653–657, 2012.

[18] Edmund Leary, Bart Limburg, Asma Alanazy, Sara Sangtarash, Iain Grace, Katsutoshi Swada, Louisa J. Esdaile, Mohammed Noori, M. Teresa González, Gabino Rubio-Bollinger, Hatef Sadeghi, Andrew Hodgson, Nicolás Agrait, Simon J. Higgins, Colin J. Lambert, Harry L. Anderson, and Richard J. Nichols. Bias-driven conductance increase with length in porphyrin tapes. *Journal of the American Chemical Society*, 140(40):12877–12883, 2018. PMID: 30207150.

[19] Zhen-Fei Liu, Sujun Wei, Hongsik Yoon, Olgun Adak, Ingrid Ponce, Yivan Jiang, Woo-Dong Jang, Luis M. Campos, Latha Venkataraman, and Jeffrey B. Neaton. Control of single-molecule junction conductance of porphyrins via a transition-metal center. *Nano Letters*, 14(9):5365–5370, 2014. PMID: 25111197.

[20] Zhihai Li, Manuel Smeu, Mark A. Ratner, and Eric Borguet. Effect of anchoring groups on single molecule charge transport through porphyrins. *The Journal of Physical Chemistry C*, 117(29):14890–14898, 2013.

[21] Mickael L. Perrin, Ferry Prins, Christian A. Martin, Ahson J. Shaikh, Rienk Eelkema, Jan H. van Esch, Tomas Briza, Robert Kaplanek, Vladimir Kral, Jan M. van Ruitenbeek,

Herre S. J. van der Zant, and Diana Dulić. Influence of the chemical structure on the stability and conductance of porphyrin single-molecule junctions. *Angewandte Chemie*, 123(47):11419–11422, 2011.

[22] Zhihai Li and Eric Borguet. Determining charge transport pathways through single porphyrin molecules using scanning tunneling microscopy break junctions. *Journal of the American Chemical Society*, 134(1):63–66, 2012. PMID: 22133080.

[23] Mohammed Noori, Albert C. Aragonès, Giuseppe Di Palma, Nadim Darwish, Steven W. D. Bailey, Qusiy Al-Galiby, Iain Grace, David B. Amabilino, Arántzazu González-Campo, Ismael Díez-Pérez, and Colin J. Lambert. Tuning the electrical conductance of metalloporphyrin supramolecular wires. *Scientific Reports*, 6:37352 EP, Nov 2016. Article.

[24] R. C. Yu, N. Tea, M. B. Salamon, D. Lorents, and R. Malhotra. Thermal conductivity of single crystal c_{60}. *Phys. Rev. Lett.*, 68:2050–2053, Mar 1992.

[25] S. Tanuma, C. J. Powell, and D. R. Penn. Calculations of electron inelastic mean free paths. v. data for 14 organic compounds over the 50–2000 ev range. *Surface and Interface Analysis*, 21(3):165–176, 3 1994.

[26] Marc Baldo. 6.701 introduction to nanoelectronics, Spring 2010. Massachusetts Institute of Technology: MIT OpenCourseWare.

[27] S. Datta. Tutorial: Electrical resistance: an atomistic view. *Nanotechnology*, 15:S433–S451, July 2004.

[28] R. Landauer. Spatial variation of currents and fields due to localized scatterers in metallic conduction. *IBM Journal of Research and Development*, 1(3):223–231, July 1957.

[29] Yoseph Imry and Rolf Landauer. Conductance viewed as transmission. *Rev. Mod. Phys.*, 71:S306–S312, Mar 1999.

[30] R. Frisenda. *OPE3: A Model System for Single-molecule Transport*. TUDelft, Applied Sciences, QN/Quantum Nanoscience, 2016. `https://doi.org/10.4233/uuid:32f64600-9075-4493-adc5-72b602944f92`.

[31] D. Stefani. *Various aspects of quantum transport through single molecules: Amechanical break-junction study*. TUDelft, Applied Sciences, QN/Quantum Nanoscience, 2019. `https://doi.org/10.4233/uuid:f6120a10-0a29-43f8-b900-bb62c856e74b`.

[32] Pascal Gehring, Jos M. Thijssen, and Herre S. J. van der Zant. Single-molecule quantum-transport phenomena in break junctions. *Nature Reviews Physics*, 1(6):381–396, 2019.

[33] John G. Simmons. Generalized formula for the electric tunnel effect between similar electrodes separated by a thin insulating film. *Journal of Applied Physics*, 34(6):1793–1803, 1963.

[34] Jacqueline Munoz. Electrical characterization of protein networks and inorganic

nanoparticles, 2018.

[35] C.A. Martin. *Charge transport through single molecules in two- and three-terminal mechanical break junctions*. TUDelft, Applied Sciences, QN/Quantum Nanoscience, 2010. http://resolver.tudelft.nl/uuid:a86dc085-6a88-4368-8fa6-7aa15bfa90f0.

[36] Christian A. Martin, Roel H. M. Smit, Ruud van Egmond, Herre S. J. van der Zant, and Jan M. van Ruitenbeek. A versatile low-temperature setup for the electrical characterization of single-molecule junctions. *Review of Scientific Instruments*, 82(5):053907, 2011.

[37] C. Untiedt, A. I. Yanson, R. Grande, G. Rubio-Bollinger, N. Agraït, S. Vieira, and J.M. van Ruitenbeek. Calibration of the length of a chain of single gold atoms. *Phys. Rev. B*, 66:085418, Aug 2002.

[38] C. Nef. *Contacting strategies for molecular electronics*. University of Basel, Faculty of Science, 2018. http://edoc.unibas.ch/diss/DissB_10885.

[39] Davide Stefani, Cristian A. Gutiérrez-Cerón, Daniel Aravena, Jacqueline Labra-Muñoz, Catalina Suarez, Shuming Liu, Monica Soler, Luis Echegoyen, Herre S. J. van der Zant, and Diana Dulic. Charge transport through a single molecule of trans-1-bis-diazofluorene [60]fullerene. *Chemistry of Materials*, 29(17):7305–7312, Sep 2017.

[40] Alvaro Etcheverry-Berríos, Ignacio Olavarría, Mickael L. Perrin, Raúl Díaz-Torres, Domingo Jullian, Ingrid Ponce, José H. Zagal, Jorge Pavez, Sergio O. Vásquez, Herre S. J. van der Zant, Diana Dulić, Núria Aliaga-Alcalde, and Monica Soler. Multiscale approach to the study of the electronic properties of two thiophene curcuminoid molecules. *Chemistry - A European Journal*, 22(36):12808–12818, 8 2016.

[41] Mario Lemmer, Michael S. Inkpen, Katja Kornysheva, Nicholas J. Long, and Tim Albrecht. Unsupervised vector-based classification of single-molecule charge transport data. *Nature Communications*, 7:12922 EP –, Oct 2016. Article.

[42] Alex Rodriguez and Alessandro Laio. Clustering by fast search and find of density peaks. *Science*, 344(6191):1492–1496, 2014.

[43] Ben H. Wu, Jeffrey A. Ivie, Tyler K. Johnson, and Oliver L. A. Monti. Uncovering hierarchical data structure in single molecule transport. *The Journal of Chemical Physics*, 146(9):092321, 2017.

[44] Damien Cabosart, Maria El Abbassi, Davide Stefani, Riccardo Frisenda, Michel Calame, Herre S. J. van der Zant, and Mickael L. Perrin. A reference-free clustering method for the analysis of molecular break-junction measurements. *Applied Physics Letters*, 114(14):143102, 2019.

[45] J. MacQueen. Some methods for classification and analysis of multivariate observations. In *Proceedings of the Fifth Berkeley Symposium on Mathematical Statistics and Probability, Volume 1: Statistics*, pages 281–297, Berkeley, Calif., 1967. University of California Press.

[46] S. Lloyd. Least squares quantization in pcm. *IEEE Transactions on Information Theory*, 28(2):129–137, March 1982.

[47] Jake VanderPlas. *Python Data Science Handbook*. O'Reilly Media, Inc., 2016. Chapter 5: Machine learning.

[48] Ernst Kussul and Tatiana Baidyk. Improved method of handwritten digit recognition tested on mnist database. *Image and Vision Computing*, 22(12):971 – 981, 2004. Proceedings from the 15th International Conference on Vision Interface.

[49] David Robinson. K-means clustering is not a free lunch, Jan 2015.

[50] Yordan P. Raykov, Alexis Boukouvalas, Fahd Baig, and Max A. Little. What to do when k-means clustering fails: A simple yet principled alternative algorithm. *PLOS ONE*, 11(9):1–28, 09 2016.

[51] Diego Lopez Yse. The anatomy of k-means: A complete guide to k-means clustering algorithm, Feb 2019.

[52] Maria El Abbassi, Patrick Zwick, Alfredo Rates, Davide Stefani, Alessandro Prescimone, Marcel Mayor, Herre S.J. van der Zant, and Diana Dulić. Unravelling the conductance path through single-porphyrin junctions. *Chem. Sci.*, pages –, 2019.

[53] Riccardo Frisenda, Davide Stefani, and Herre S. J. van der Zant. Quantum transport through a single conjugated rigid molecule, a mechanical break junction study. *Accounts of Chemical Research*, 51(6):1359–1367, 2018.

[54] Edmund Leary, Bart Limburg, Asma Alanazy, Sara Sangtarash, Iain Grace, Katsutoshi Swada, Louisa J. Esdaile, Mohammed Noori, M. Teresa González, Gabino Rubio-Bollinger, Hatef Sadeghi, Andrew Hodgson, Nicolás Agraít, Simon J. Higgins, Colin J. Lambert, Harry L. Anderson, and Richard J. Nichols. Bias-driven conductance increase with length in porphyrin tapes. *Journal of the American Chemical Society*, 140(40):12877–12883, 2018.

[55] R. Frisenda, S. Tarkuç, E. Galán, M. L. Perrin, R. Eelkema, F. C. Grozema, and H. S. J. van der Zant. Electrical properties and mechanical stability of anchoring groups for single-molecule electronics. *Beilstein J. Nanotechnol.*, 6:1558—-1567, 2015.

Appendix A

Conductance values and clustering results

In figures A.1, A.2 and A.3 the complete classes sets are presented for molecules P1, R1 and R3 in order to compare the different classes obtained after the clustering analysis. Figure A.1 presents the classes obtained after applying the cluster analysis to the measurements of molecule P1. Four classes corresponding to Class A, Class B, Class C and the tunneling class are present. In figure A.2, the two classes corresponding to molecule R1 are shown. These classes are attributed to Class C and the tunneling class. Finally, in figure A.3, three classes are displayed for the case of molecule R3, attributed to Class B, Class C and the tunneling class. Notice that Class B, although have a similar conductance peak as P1, is more slanted. Molecule R2 presents only tunneling traces.

Table A.1 shows a summary of the fitting of the conductance peak of the three different classes. The Full Width Half Maximum (FWHM), yield and length of every measured molecule attributed to each class is presented. Table S2 presents a summary of all the measurements performed in this study. In the table A.2, the number of samples, junctions and traces is shown for different bias voltage and bending speed. Each sample has a maximum of 4 junctions.

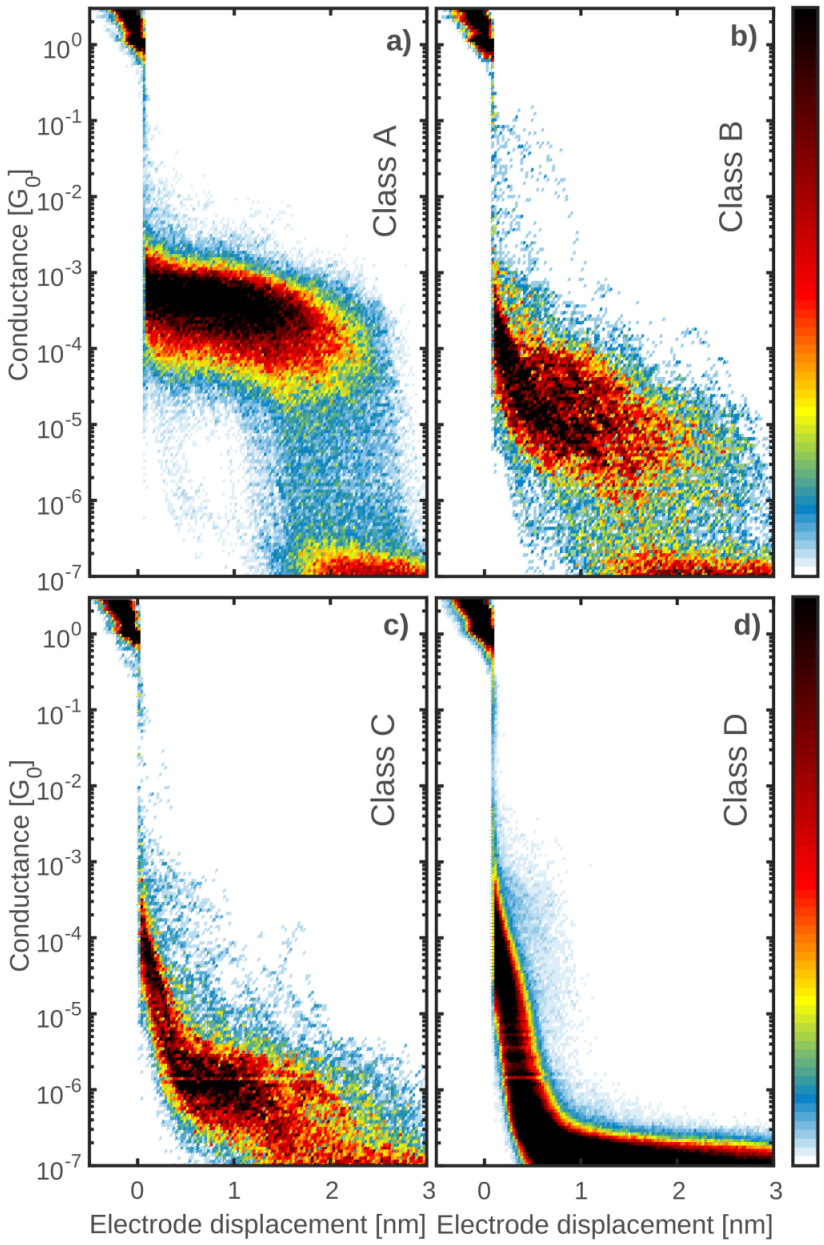

Figure A.1: Two-dimensional histograms of the complete data from P1. Four different categories of breaking traces are shown corresponding to a) Class A (7.9%), b) class B (2.0%), c) class C (2.7%) and d) class D with no clear molecular signature (84.7%).

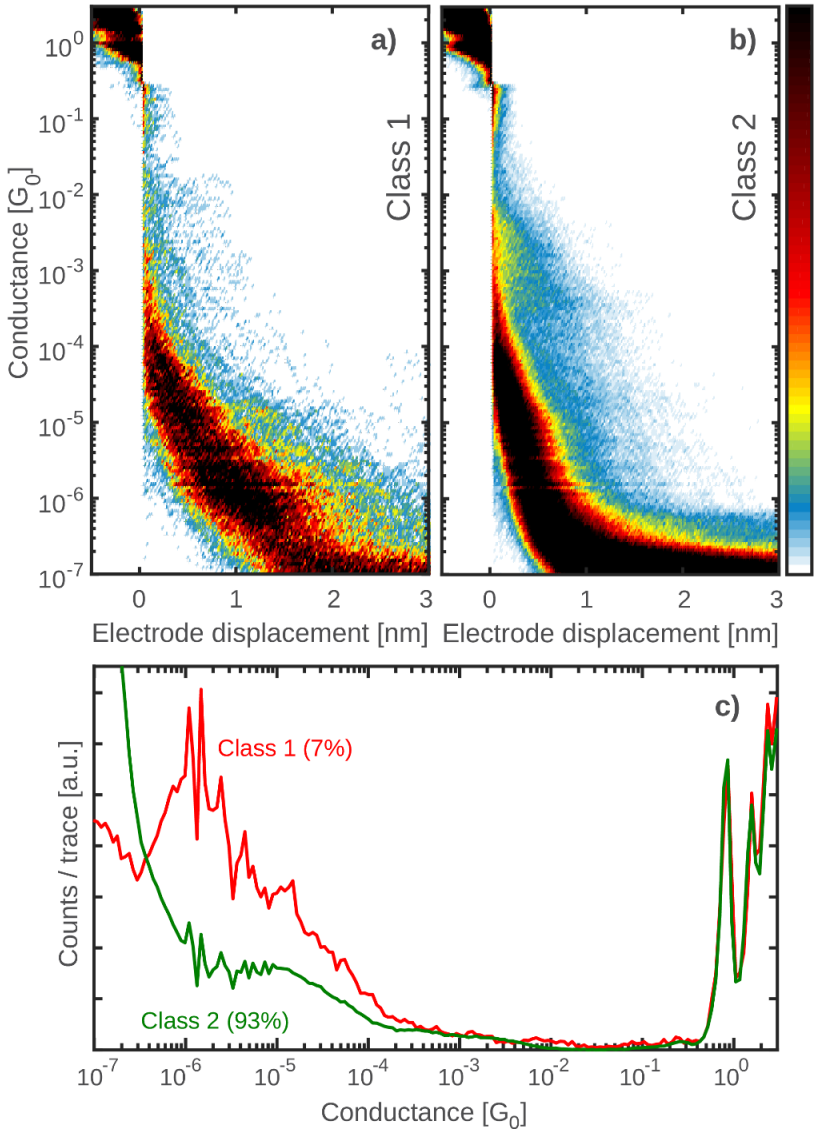

Figure A.2: Two-dimensional histograms of the complete data from R1. Two different categories of breaking traces are shown corresponding to a) Class 1 (7%) and b) class 2 (93%) with no clear molecular signature. d) 1D conductance histogram for class 1 and 2.

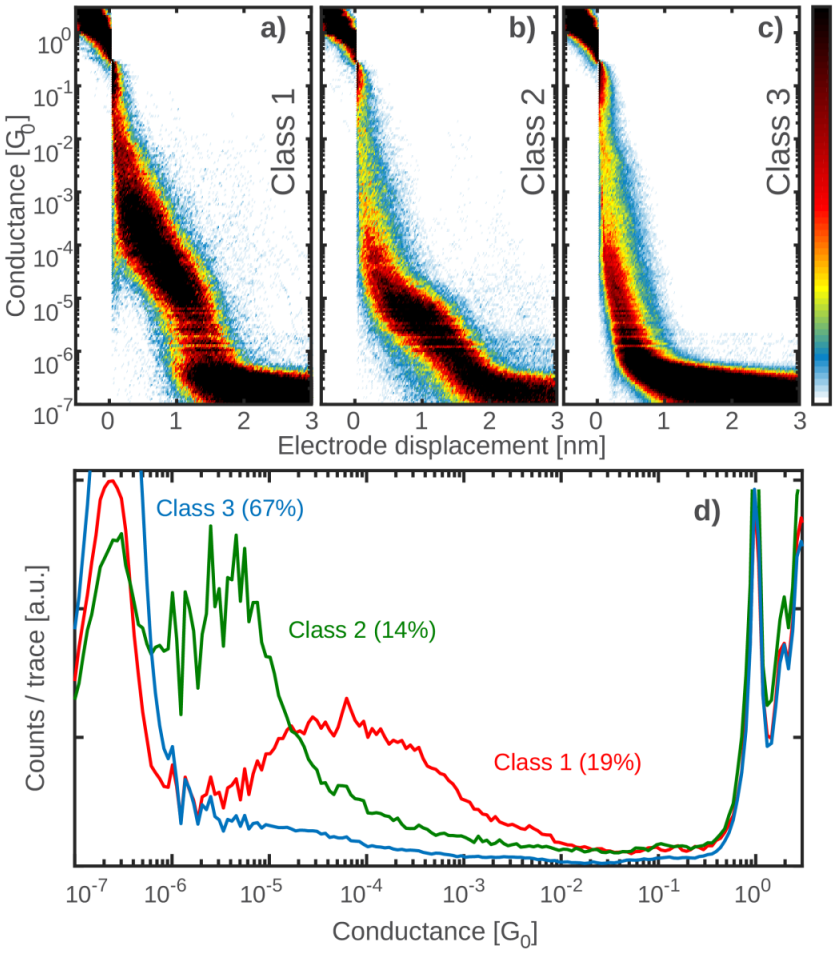

Figure A.3: Two-dimensional histograms of the complete data from R3. Three different categories of breaking traces are shown corresponding to a) Class 1 (19%), b) class 2 (14%) and c) class 3 (67%) with no clear molecular signature. d) 1D conductance histogram for class 1, class 2 and class 3.

		P1	**R1**	**R2**	**R3**	**ZnP1**	**P2**	**P3**
Class A	$G_M(G_0)$	2.80E-04	-	-	-	2.40E-04	1.90E-04	2.30E-04
	FWHM	1.1	-	-	-	1.8	1.2	0.8
	Yield	7.90%	-	-	-	12.00%	7.10%	6.40%
	L(nm)	1.9	-	-	-	2	1.8	2.2
Class B	$G_M(G_0)$	1.10E-05	-	-	5.10E-05	2.10E-05	4.00E-05	8.30E-06
	FWHM	1.5	-	-	2.4	1.7	1.2	0.9
	Yield	2.00%	-	-	19.00%	4.10%	7.10%	1.00%
	L(nm)	1.8	-	-	1	1.5	1.8	2
Class C	$G_M(G_0)$	1.00E-06	2.80E-06	-	1.20E-06	4.10E-06	1.70E-06	1.00E-06
	FWHM	1	1.6	-	2	1.9	1.7	0.6
	Yield	2.70%	14.00%	-	7.00%	16.20%	4.70%	0.30%
	L(nm)	2	1	-	1.5	1.1	1.8	2.3

Table A.1: Conductance peak, full width half maximum (FWHM), yield and length extracted from the clustering analysis and the 1D histogram fitting for each class on every molecule measured, related to each class.

Molecule	Sample	Junction	Bias (V)	Bending speed (nm/s)	Traces
P1	1	1	0.1	6×10^4	20 000
			0.1	6×10^4	5 000
		2	0.1	6×10^4	9 589
	2	1	0.1	6×10^4	10 000
		2	0.1	6×10^4	10 000
Total	**2**	**4**			**54 589**
R2	1	1	0.1	6×10^4	20 000
			0.2	6×10^4	10 000
Total	**1**	**1**			**30 000**
R1	1	1	0.1	6×10^4	10 000
			0.2	6×10^4	10 000
			0.3	6×10^4	10 000
Total	**1**	**1**			**30 000**
R3	1	1	0.1	6×10^4	4 994
		2	0.1	6×10^4	17 271
Total	**1**	**2**			**22 265**
ZnP1	1	1	0.1	6×10^4	5 000
			0.1	3×10^4	5 000
		2	0.1	6×10^4	20 000
			0.2	6×10^4	5 000
	2	1	0.1	6×10^4	20 000
			0.2	6×10^4	10 000
			0.3	6×10^4	8 280
Total	**1**	**2**			**73 280**
P2	1	1	0.1	6×10^4	8 376
		2	0.1	6×10^4	10 000
	2	1	0.1	3×10^4	3 083
	3	1	0.1	3×10^4	9 236
	4	1	0.1	3×10^4	14 835
	5	1	0.1	3×10^4	5 000
Total	**5**	**6**			**50 530**
P3	1	1	0.2	6×10^4	10 000
			0.1	6×10^4	20 000
	2	1	0.1	6×10^4	5 000
Total	**2**	**2**			**25 000**
Total of traces	**285 664**				

Table A.2: Number of samples, junctions and traces measured with the different parameters (bias and bending speed) for the different molecules. All the comparisons presented in this paper are using 10 000 traces with a bias of 100 mV and a speed of 6×10^4 nm/s.

Chemical Science

EDGE ARTICLE

View Article Online
View Journal

Cite this: DOI: 10.1039/c9sc02497b

All publication charges for this article have been paid for by the Royal Society of Chemistry

Unravelling the conductance path through single-porphyrin junctions†

Maria El Abbassi, ‡[a] Patrick Zwick,‡[b] Alfredo Rates,[ac] Davide Stefani,[a] Alessandro Prescimone,[b] Marcel Mayor,*[bde] Herre S. J. van der Zant*[a] and Diana Dulić*[c]

Received 22nd May 2019
Accepted 30th July 2019

DOI: 10.1039/c9sc02497b

rsc.li/chemical-science

Porphyrin derivatives are key components in natural machinery enabling us to store sunlight as chemical energy. In spite of their prominent role in cascades separating electrical charges and their potential as sensitizers in molecular devices, reports concerning their electronic transport characteristics are inconsistent. Here we report a systematic investigation of electronic transport paths through single porphyrin junctions. The transport through seven structurally related porphyrin derivatives was repeatedly measured in an automatized mechanically controlled break-junction set-up and the recorded data were analyzed by an unsupervised clustering algorithm. The correlation between the appearances of similar clusters in particular sub-sets of the porphyrins with a common structural motif allowed us to assign the corresponding current path. The small series of model porphyrins allowed us to identify and distinguish three different electronic paths covering more than four orders of magnitude in conductance.

1 Introduction

Porphyrins and their related macrocycles are promising building blocks for the construction of functional molecular devices, as their rich and tunable optical and electrical properties can be employed in a wide range of applications, including those in catalysis, electrocatalysis, solar energy conversion, and photodynamic cancer therapy.[1–6] Furthermore, porphyrin synthesis is well established, allowing us to fine tune their chemical design in order to study fundamental charge transport through single molecules.[7–9] Side groups can be added to porphyrins in a modular way, allowing us to methodically test various chemical designs with different anchoring, bulky and spacer groups.[10] Additionally, expanded porphyrins have been suggested as building blocks for electronic applications displaying rich transport variety depending on their topology.[11]

However, it has been reported that porphyrin molecules have a low conductance value of the order of 1×10^{-5} G_0, albeit with a low β-attenuation factor especially at higher bias voltages,[12,13] with only a few studies recording higher conductance ($\approx 1 \times 10^{-4}$ G_0).[14,15] The extensive π-system enables the formation of molecular junctions with different stable configurations, leading to a large spread in conductance.[16,17] Studies about the influence of a coordinating metal show that the presence of a central ion hardly alters the conductance of the parent porphyrin structure.[18] However, the incorporation of Zn can induce conformational changes that lead to the appearance of an additional conducting state.[18] This rich variety of structural aspects reflected in their transport behaviour makes porphyrins interesting model compounds, but limits their potential for applications. These limitations could be overcome by an optimization of the molecular design, however the identification and characterization of the possible conductance paths at the single molecule level is required for this.

In this study, we systematically investigate transport across porphyrin-based compounds in order to identify the influence of structural features. In particular, the presence of anchoring groups, the bulkiness of the substituents, the presence of a metal ion and the dimension of the π-system are correlated with the recorded transport properties. For this reason, we synthesized seven different compounds with closely related geometry features, and measured them using an automatized mechanically controlled break-junction technique (MCBJ). By employing an unsupervised clustering algorithm[19,20] on a unique set of data consisting of almost 100 000 conductance traces, we identify classes of common behaviours in the

[a]Kavli Institute of Nanoscience, Delft University of Technology, 2600 GA Delft, The Netherlands. E-mail: h.s.j.vanderzant@tudelft.nl

[b]Department of Chemistry, University of Basel, CH-4056 Basel, Switzerland. E-mail: marcel.mayor@unibas.ch

[c]Department of Physics, Department of Electrical Engineering, Faculty of Physical and Mathematical Sciences, University of Chile, Avenida Blanco Encalada 2008, Santiago 8330015, Chile. E-mail: ddulic@ing.uchile.cl

[d]Institute of Nanotechnology (INT), Karlsruhe Institute of Technology (KIT), D-76021 Karlsruhe, Germany

[e]Lehn Institute of Functional Materials (LIFM), School of Chemistry, Sun Yat-Sen University (SYSU), Guangzhou 510275, China

† Electronic supplementary information (ESI) available. CCDC 1910499–1910507. For ESI and crystallographic data in CIF or other electronic format see DOI: 10.1039/c9sc02497b

‡ These authors contributed equally to this work.

breaking traces and their correlation with structural features of the molecules under investigation enables us to link each of them to a different electron pathway across the porphyrins.

2 Experimental

The chemical structure of the porphyrin molecules included in this study can be found in Fig. 1a and b. Compounds **P1**, **P2** and **P3** share the same linear backbone, consisting of the porphyrin core, phenylene–acetylene spacers and thiol anchoring groups, but vary in their lateral bulky groups. With this series, the influence of the steric requirement of the peripheral phenyl subunit shall be studied. **ZnP1**, a variant of **P1** which includes a Zn(II) ion in the porphyrin core, is employed to investigate variations in the transport characteristics emerging from the presence of the metal center.

The role of the anchoring groups and of the spacers is investigated by comparing the results of **P1** with those obtained from three derivatives that possess the same lateral bulky groups, but have different components in their backbones (Fig. 1b): **R1** exposes only on one side the backbone structure of **P1** comprising a thiol anchor group, **R2** has neither acetylene spacers nor anchoring groups, whereas **R3** has a similar backbone to **P1**, but with terminal *tert*-butyl groups replacing the thiol anchoring groups.

Samples consist of a thin gold constriction suspended on top of a flexible substrate coated with an insulating layer of polyimide, as depicted in Fig. 1c. The sample is mounted in a three-point bending mechanism, clamped between two lateral supports and the head of a central pushing rod. Upon bending, the gold wire stretches until rupture, which leaves two atomically sharp electrodes whose separation can be adjusted mechanically. The wire can be fused back by reducing the deformation of the substrate. The breaking–making process can be repeated thousands of times while the conductance of the junction is recorded. A two-dimensional (2D) histogram of the conductance *vs.* displacement is built from the "breaking traces". The measurements were performed in an MCBJ setup at room temperature in air. All the measurements presented in this work have been performed with a bias voltage of 100 mV. Each dataset presented in this work consists of 10 000 consecutive traces recorded on the same junction and without data selection.

3 Synthesis

The porphyrin model compounds studied in this work were synthesised by variations of reported procedures, which are summarized in Fig. 2.[21,22] The porphyrin subunits of **R2** and the intermediates **1**, **2**, and **3** were assembled from the corresponding bis-pyrroles and aldehydes. For the precursor **7** of the mono-functionalized porphyrin, both aldehydes were used in equal amounts. Condensation of literature-known 2,2′-((4-(*tert*-butyl)phenyl)methylene)bis(1*H*-pyrrole)[23] with either 4-(*tert*-butyl)benzaldehyde or commercially available 3-(trimethylsilyl) propiolaldehyde provided **R2** or **1** respectively. Using instead either 2,2′-((3,5-di-*tert*-butylphenyl)methylene)bis(1*H*-pyrrole)[24] or 2,2′-(mesitylmethylene)bis(1*H*-pyrrole)[21] in combination with 3-(trimethylsilyl)propiolaldehyde provided **2** and **3** respectively. The less symmetric **7** was condensed from a 2/1/1 mixture of 2,2′-((4-(*tert*-butyl)phenyl)methylene)bis(1*H*-pyrrole),[23] 4-(*tert*-butyl)benzaldehyde, and 3-(triisopropylsilyl)propiolaldehyde.[25] For the condensation reactions, a protocol of Anderson *et al.* was adapted, which was already used for the preparation of literature-known **2**.[26]

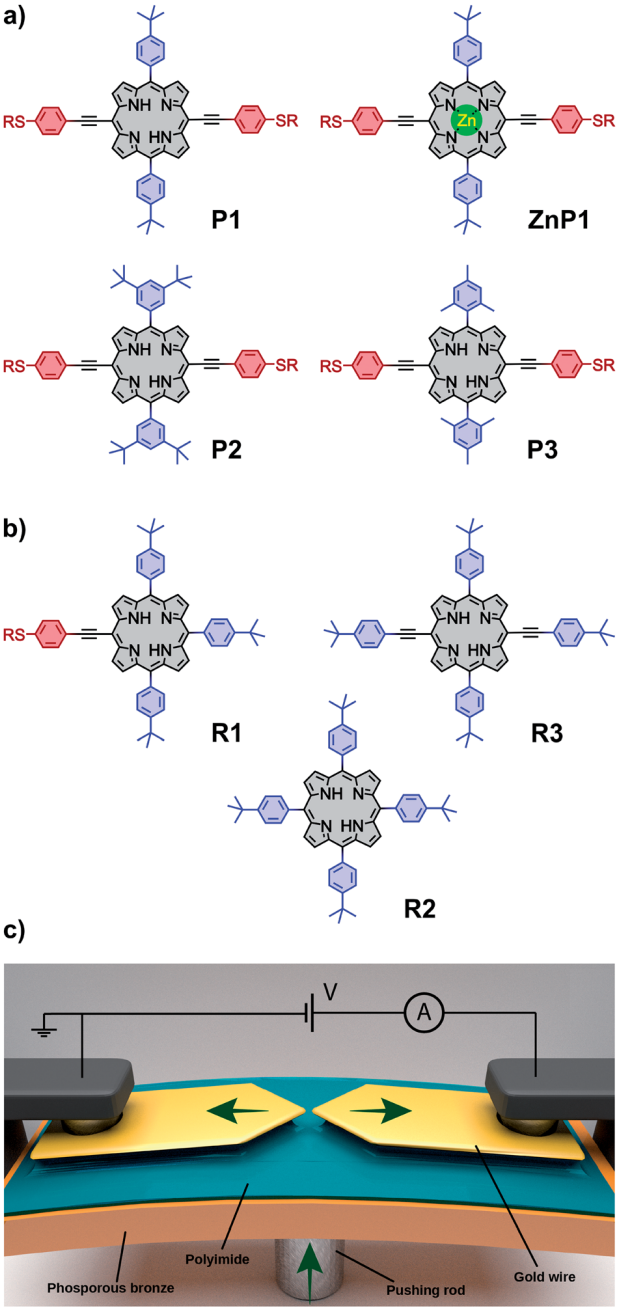

Fig. 1 (a) Structural designs of **P1**, **ZnP1**, **P2** and **P3**; (b) structural formula of **R1**, **R2** and **R3**. The different parts of the molecule have been coloured dividing the anchoring groups (red) and the bulky side groups (blue). The molecules are synthesized with R = acetyl, but upon deprotection at the electrode surface, R represents either a hydrogen atom or the gold electrode. (c) Schematics of the mechanically controllable break-junction (MCBJ) setup.

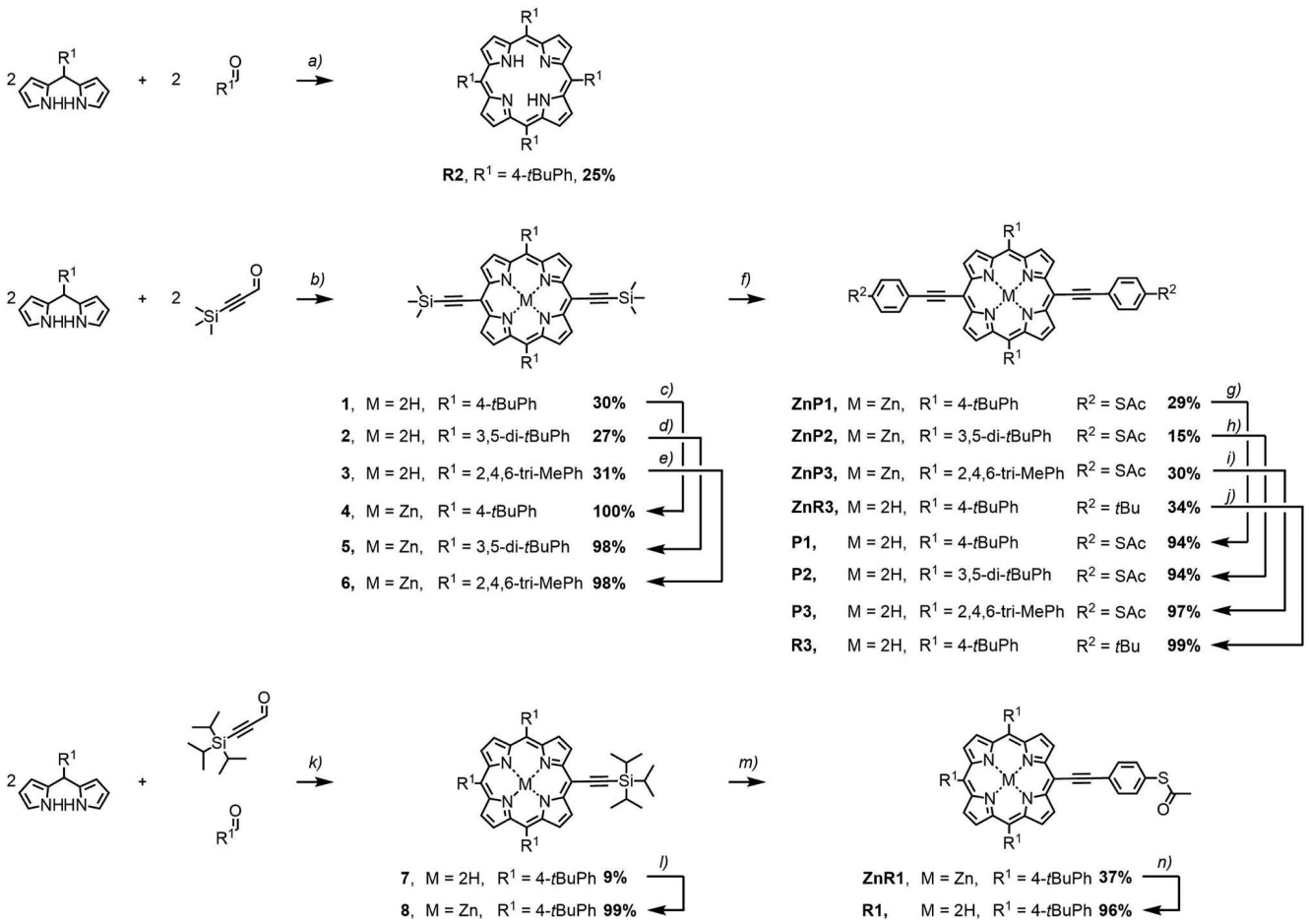

Fig. 2 Synthetic overview. (a) (1) $BF_3 \cdot OEt_2$, CH_2Cl_2, rt, 45 min. (2) DDQ, CH_2Cl_2, rt, 1 h. (b) (1) $BF_3 \cdot OEt_2$, CH_2Cl_2, 0 °C rt, 5 20 min. (2) DDQ, CH_2Cl_2, rt, 1 h. (c–e) $Zn(OAc)_2$, CH_2Cl_2, CH_3OH, rt, 1 h to 3 d. (f) (1) TBAF, 2Me-THF, rt, 1 h. (2) *S*-(4-Iodophenyl)ethanethioate, $Pd(PPh_3)_4$, CuI, THF, NEt_3, rt, 1–16 h. (g–j) TFA, CH_2Cl_2, rt, 2 h. (k) (1) $BF_3 \cdot OEt_2$, CH_2Cl_2, rt, 5 min. (2) DDQ, CH_2Cl_2, rt, 1 h. (l) $Zn(OAc)_2$, CH_2Cl_2, CH_3OH, rt, 1 h. (m) (1) TBAF, 2Me-THF, rt, 1 h. (2) *S*-(4-Iodophenyl)ethanethioate, $Pd(PPh_3)_4$, CuI, THF, NEt_3, rt, 16 h. (n) TFA, CH_2Cl_2, rt, 2 h.

Condensation reactions were catalysed by $BF_3 \cdot OEt_2$ in CH_2Cl_2 at either 0 °C or room temperature for 5 to 45 minutes prior to oxidation by 2,3-dichloro-5,6-dicyano-*p*-benzoquinone (DDQ) at room temperature for one hour. The c_2 symmetric porphyrins **R2**, **1**, **2** and **3** were isolated in typical yields of 27 to 31%. The less symmetric compound **7** was condensed in a statistic fashion leading to 9% yield. Metalation of the porphyrins by zinc(II) acetate in a CH_2Cl_2/CH_3OH mixture for one hour to three days at room temperature provided the Zn–porphyrins **4**, **5**, **6**, and **8** almost quantitatively.

Further functionalization of the porphyrins **4–6** required the liberation of the alkyne group, which was achieved by treatment with tetrabutylammonium fluoride (TBAF) at room temperature for one hour in 2-methyltetrahydrofuran (2Me-THF). Without further purification, these compounds were engaged in Sonogashira–Hagihara cross couplings[22] with excesses of the iodoaryls of interest. The coupling reaction was performed in dry and degassed THF and NEt_3 with $Pd(PPh_3)_4$ and CuI as catalysts at room temperature with reaction periods between 2 and 16 hours. Using *S*-(4-iodophenyl)ethanethioate as iodoaryl gave access to **ZnP1** in isolated yields of 29%. Treatment with trifluoroacetic acid (TFA) in CH_2Cl_2 for two hours at room temperature gave the free base analogues **P1**, **P2**, **P3**, **R1**, and **R3** almost quantitatively.

The identity of all porphyrin derivatives was corroborated by ^{1}H-NMR spectroscopy and mass spectrometry. In addition, single crystals suitable to analyse the solid state structure by X-ray diffraction were obtained for **1**, **2**, **3**, **4**, **5**, **ZnP1**, **P2**, and **R2**. A sulphur-to-sulphur distance of 2.41 nm could be extracted from the crystallographic data of **ZnP1** and **P2**, showing independence of the structural variations, such as bulky groups or the incorporated Zn(II) ion (Fig. 3). Detailed description of the experimental procedures and the analytical data of all the compounds are provided as ESI.†

4 Results

Fig. 4a and b show the 2D histograms of two representative measurements performed on **P1** and **R2**, respectively. While for **P1** a clear plateau is found above 1×10^{-4} G_0 and extending for about 2 nm (Fig. 4a), no clear plateau is observed in the case of **R2**. Examples of individual breaking traces recorded for each molecule are presented in Fig. 4c and d. Clear and flat plateaus above 1×10^{-4} G_0 are observed in the case of **P1**, whereas, in the case of **R2**, the plateau is absent. All the molecules containing

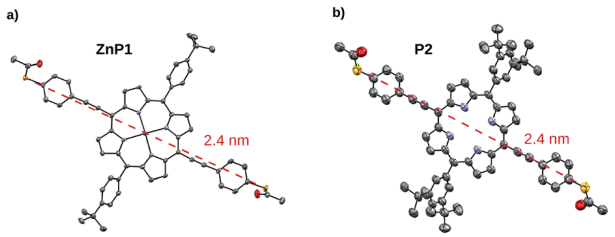

Fig. 3 ORTEP-representation of solid-state structures. (a) **P2** and (b) **ZnP1**. Thermal ellipsoids are plotted at a 50% probability level. The dashed red line displays the main axis and the S–S distance.

two thiol groups as anchoring sites (**P1**, **P2**, **P3**, **ZnP1**) show a similar conductance histogram to that in Fig. 4a with a very well-defined plateau, in contrast to the measurements of the reference molecules **R1**, **R2** and **R3** which lack this design feature (see Fig. S1†).

To further investigate the charge transport pathways, an unsupervised clustering algorithm has been used to subdivide the different datasets in four different classes.[20] Classes A–C are associated with the presence of a molecule inside the junction, whereas class D (see Fig. S2†) contains the traces in which no molecular junction has been formed and only shows the exponential decay typical of tunnelling that occurs through a barrier. The results obtained for **P1** are reported in Fig. 5, as an example. Class A constitutes 64.7% of the molecular junctions and contains the traces that exhibit a plateau of about 2.2 nm length. A log-normal fit to the peak in the 1D conductance histogram reveals it being centred around 2×10^{-4} G_0 (red colored high-conductance area in Fig. 5c). The traces grouped in class B (28.8%) form a slightly shorter and wider plateau, centred at 3×10^{-5} G_0 (green colored medium-conductance class in Fig. 5c). Finally, class C (6.5%) shows a broad feature centred at 2×10^{-6} G_0 (blue in Fig. 5d). The three classes together constitute 12.6% of the total traces. The same clustering analysis has been applied to all the datasets and four groups with similar features have been found. Table 1 summarizes the occurrence of each class for the various molecules.

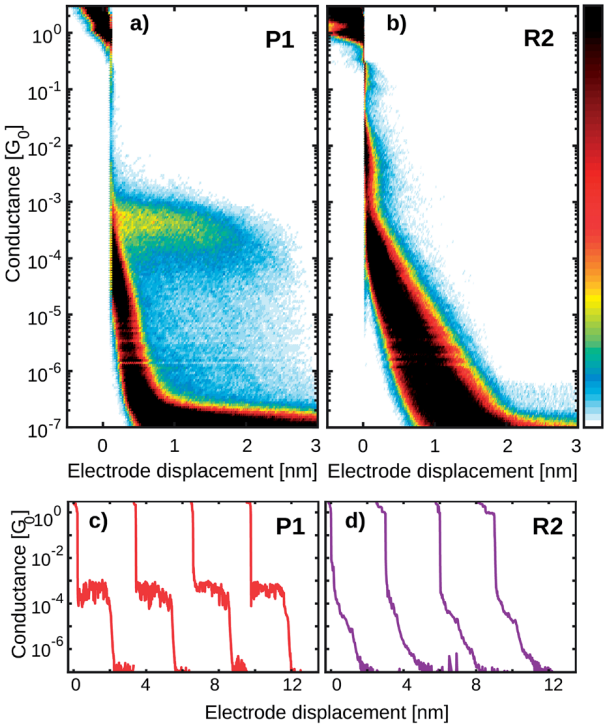

Fig. 4 Two-dimensional conductance *vs.* displacement histograms built from 10 000 consecutive breaking traces of (a) **P1** and (b) **R2**; no data selection was made. Both measurements were performed with a bias of 100 mV at room temperature. Examples of individual conductance breaking traces for (c) **P1** and (d) **R2** (with a horizontal offset of 3 nm for clarity).

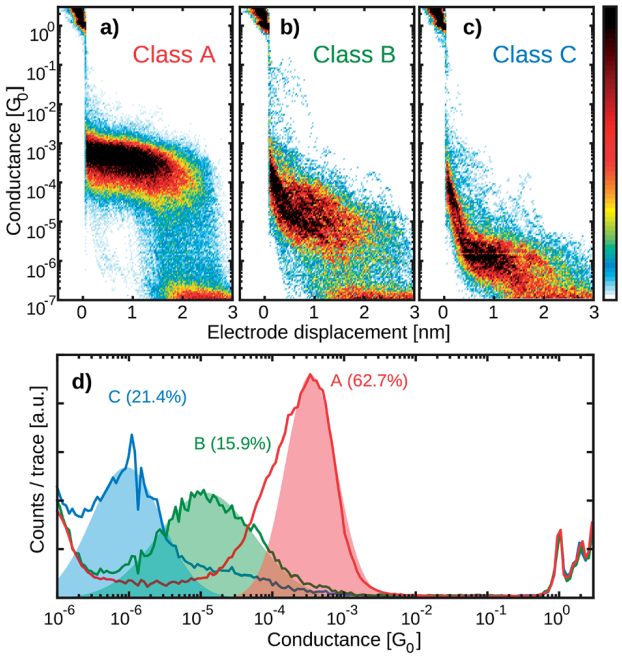

Fig. 5 Clustering analysis of the conductance properties of **P1**. (a–c) Two-dimensional histograms of the three different categories of breaking traces obtained from the reference-free cluster analysis applied to **P1**. (d) One-dimensional conductance histograms corresponding to classes A, B and C. By fitting a log-normal distribution to the one-dimensional histograms, we can extract the conductance peak positions at 2×10^{-4} G_0 for class A (64.7% of the molecular traces), 3×10^{-5} G_0 for class B (28.8%) and 2×10^{-6} G_0 in the case of class C (6.5%).

Table 1 Summary of the occurrence of the three molecular classes for each molecule. Class A corresponds to the high-conductance class, class B corresponds to the medium-conductance class and class C corresponds to the low-conductance class

Molecule	Class A	Class B	Class C
P1	✓	✓	✓
P2	✓	✓	✓
P3	✓	✓	✓
ZnP1	✓	✓	✓
R1			✓
R2			
R3		✓	✓

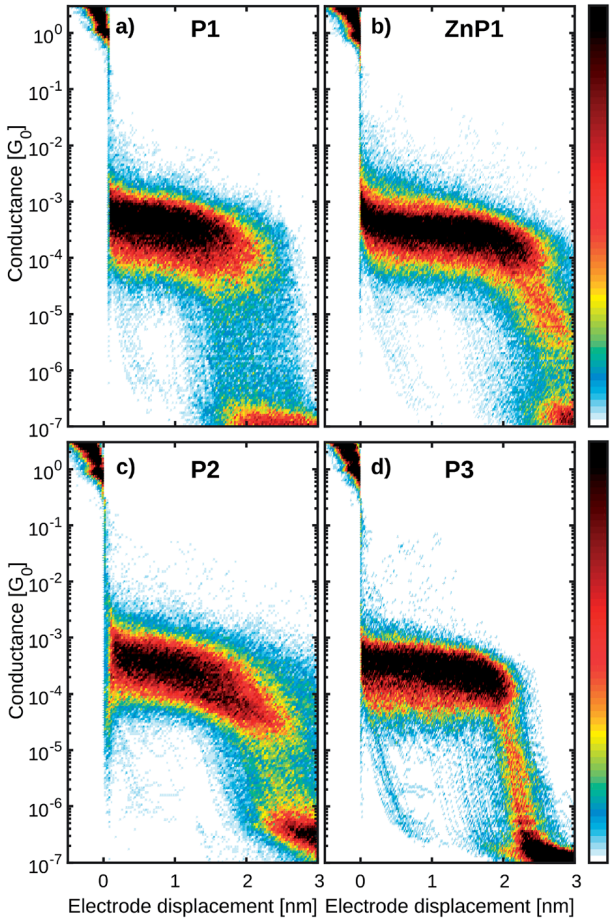

Fig. 6 Two-dimensional conductance *vs.* displacement histograms for (a) **P1**, (b) **ZnP1**, (c) **P2** and (d) **P3**. The histograms only include breaking traces with the behaviour present in class A. All datasets have similar length and conductance values.

5 Discussion

While class A is present only in the four compounds containing two thiol anchoring groups (**P1**, **P2**, **P3** and **ZnP1**), class B is also found in **R3**. Class C, on the other hand, is present in all the measurements except those of **R2**. The 2D conductance histograms of class A obtained in the case of the molecules containing the same backbone exposing two terminal thiol groups (**P1**, **ZnP1**, **P2** and **P3**) are displayed in Fig. 6. The observed differences in plateau conductance or length are within the variations typically found in MCBJ experiments even when performed on the same molecule.[27] For this reason, we attribute this feature to the junction configuration in which the molecule is connected to both electrodes *via* the thiols and transport occurs from sulfur to sulfur. This is supported by the average trace length of about 2 nm, which is in good agreement with the estimated length from the crystallographic measurements of the sulfur-to-sulfur distance (Fig. 3). Noticeably, the presence of the Zn atom does not affect this plateau, indicating that the electron paths involved in transport are mainly localized on the aromatic system of the ligand.[12] We further note that for **P3**, class A exhibits the least slanted conductance plateau with the narrowest distribution (see Table S1†). In addition, the breaking of the molecular junction around 2 nm occurs in a more abrupt way compared to the other derivatives. In this respect, it is interesting that the bulky groups of **P3** are more spatially localized above and below the porphyrin system than for the other molecules **P1** and **P2**, thus reducing access to the π system of the porphyrin core.

The correlation of the presence/absence of particular classes with the structure of the studied porphyrin allows us to assign possible transport paths of the molecular junction (Fig. 7 and S17†). Class A is assigned to the molecule bridging the electrodes *via* the thiol anchor groups, as intended by the molecular design (Fig. 7a). The matching length of the plateau with the dimension of the structure and the fact that exclusively the porphyrins with terminal thiol-exposing backbones show that this class corroborate the assignment.

Both classes B and C are not observed for the porphyrin compound without phenylene–acetylene spacers (**R2**), suggesting that their presence introduces additional charge transport pathways. Compared to that observed in class A, the plateau in class B has a lower conductance, and it is shorter, more spread out and observed less frequently. In the case of **R3**, not containing any thiol groups, this plateau is more slanted. Hence, the presence of the thiol groups seems to stabilize the junction, yielding more defined plateaus even if the electron injection does not occur through the sulfur atom. The charge transport pathway could thus involve the acetylene spacer or the phenyl

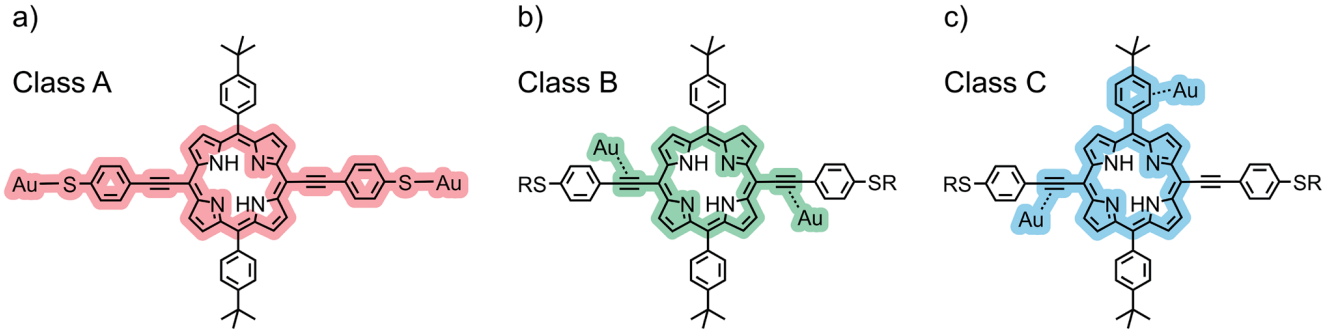

Fig. 7 Suggested transport pathways corresponding to the 3 different classes through the molecular structure displayed with **P1**. Au represents the electrode. The contact to the corresponding subunit is schematically drawn.

ring on both sides of the molecule, as it is not observed in molecules that do not contain these groups (Fig. 7b).

Class C, on the other hand, can be related to the path that results from injection in the π-system of the acetylene group and ends at one of the lateral phenyl rings (Fig. 7c). This is suggested by the fact that this class is also observed in molecule **R3** that does not have sulfur atoms in its structure but comprises the components suggested for the current path. In this case, however, the plateau is more slanted, again suggesting that the sulfur plays a role in the stability of the junction configuration. The role of sulfur in mechanically stabilizing the junction configuration is also corroborated by the reduced conductance spread in **R1**, which does expose a thiol as a potential mechanical anchor, compared to **R2** and **R3**, which do not. To check the stability of the different classes, self-breaking measurements were performed in the case of compound **P1** (see Fig. S6† for more details). While class A showed high stability (up to 5 minutes at room temperature), the lifetime of classes B and C did not exceed the tens of seconds. These observations confirm the hypothesis about the mechanical stabilization role of the thiol anchors.

The pathways attributed to classes B and C can be compared to the "*para*" and "*ortho*" paths found by Li *et al.* in the case of porphyrins without acetylene spacers and with pyridine anchoring groups.[15] While in their experiments the two pathways resulted in conductances that differed by a factor of 1.4, in our case the difference is about an order of magnitude.

Finally, apart from tunnelling traces (class D), none of the classes found in **R2** exhibits a clear molecular signature. This confirms that the bulky groups do not form an efficient injection point for charges and that the transport path from one bulky group to another is ineffective.

6 Conclusion

In this study, we report an unprecedented dataset of almost 300 000 traces measured on seven different porphyrin derivatives. We identified transport pathways by methodically and purposefully modifying the chemical design of these porphyrin-based compounds and by applying an unbiased clustering algorithm for the analysis of the breaking traces. By introducing phenylene–acetylene as the spacer and thiols as anchor groups, we achieved very stable molecular junctions with a high conductance up to 2×10^{-4} G_0. The observed high-conductance plateau is related to the thiol-to-thiol conduction path. Both, bulky groups and the Zn ion as a metal center did not have a significant influence on the junction properties, suggesting that the conductance through the molecule is mainly localized on the conjugated porphyrin system. Other classes with lower conductance were found and were related to the presence of phenylene–acetylene spacers.

Conflicts of interest

There are no conflicts to declare.

Acknowledgements

This study was supported by the EU through a RISE(DAFNEOX) project, SEP 210165479 and partially funded by the FET open project QuIET (no. 767187). The device fabrication was done at the Kavli Nanolab at Delft. DD acknowledges Fondecyt Regular Project 1181080 for financial support. Generous financial support by the Swiss National Science Foundation (SNF grant number 200020-178808) is gratefully acknowledged. M. M. acknowledges support by the 111 project (90002-18011002).

Notes and references

1 T. S. Balaban, Tailoring porphyrins and chlorins for self-assembly in biomimetic artificial antenna systems, *Acc. Chem. Res.*, 2005, **38**(8), 612–623.
2 S. Horn, K. Dahms and M. O. Senge, Synthetic transformations of porphyrins–advances 2004-2007, *J. Porphyrins Phthalocyanines*, 2008, **12**(10), 1053–1077.
3 M. Jurow, A. E. Schuckman, J. D. Batteas and C. Michael Drain, Porphyrins as molecular electronic components of functional devices, *Coord. Chem. Rev.*, 2010, **254**(19–20), 2297–2310.
4 T. D. Lash, K. M. Kadish, K. M. Smith, and R. Guilard, *The porphyrin handbook*, ed. K. M. Kadish, 2000, pp. 125–200.
5 Z. Liu, A. A. Yasseri, J. S. Lindsey and D. F. Bocian, Molecular memories that survive silicon device processing and real-world operation, *Science*, 2003, **302**(5650), 1543–1545.
6 M. L. Perrin, C. J. O. Verzijl, C. A. Martin, A. J. Shaikh, R. Eelkema, J. H. Van Esch, J. M. Van Ruitenbeek, J. M. Thijssen, H. S. J. van der Zant and D. Dulić, Large tunable image-charge effects in single-molecule junctions, *Nat. Nanotechnol.*, 2013, **8**(4), 282.
7 T. Tanaka and A. Osuka, Conjugated porphyrin arrays: synthesis, properties and applications for functional materials, *Chem. Soc. Rev.*, 2015, **44**(4), 943–969.
8 F. Moresco, G. Meyer, K.-H. Rieder, H. Tang, A. Gourdon and C. Joachim, Conformational changes of single molecules induced by scanning tunneling microscopy manipulation: A route to molecular switching, *Phys. Rev. Lett.*, 2001, **86**(4), 672.
9 O. Shoji, H. Tanaka, T. Kawai and Y. Kobuke, Single molecule visualization of coordination-assembled porphyrin macrocycles reinforced with covalent linkings, *J. Am. Chem. Soc.*, 2005, **127**(24), 8598–8599.
10 Z. Li, M. Smeu, M. A. Ratner and E. Borguet, Effect of anchoring groups on single molecule charge transport through porphyrins, *J. Phys. Chem. C*, 2013, **117**(29), 14890–14898.
11 T. Stuyver, M. Perrin, P. Geerlings, F. De Proft and M. Alonso, Conductance switching in expanded porphyrins through aromaticity and topology changes, *J. Am. Chem. Soc.*, 2018, **140**(4), 1313–1326.
12 E. Leary, B. Limburg, A. Alanazy, S. Sangtarash, I. Grace, K. Swada, L. J. Esdaile, M. Noori, M. Teresa González, G. Rubio-Bollinger, H. Sadeghi, A. Hodgson, N. Agraït, S. J. Higgins, C. J. Lambert, H. L. Anderson and

R. J. Nichols, Bias-driven conductance increase with length in porphyrin tapes, *J. Am. Chem. Soc.*, 2018, **140**(40), 12877–12883.

13 G. Sedghi, V. M. García-Suárez, L. J. Esdaile, H. L. Anderson, C. J. Lambert, M. Santiago, D. Bethell, S. J. Higgins, M. Elliott, J. Neil Bennett, E. Macdonald and R. Nichols, Long-range electron tunnelling in oligo-porphyrin molecular wires, *Nat. Nanotechnol.*, 2011, **6**(8), 517.

14 G. Sedghi, K. Sawada, L. J. Esdaile, M. Hoffmann, H. L. Anderson, D. Bethell, W. Haiss, S. J. Higgins and R. J. Nichols, Single molecule conductance of porphyrin wires with ultralow attenuation, *J. Am. Chem. Soc.*, 2008, **130**(27), 8582–8583.

15 Z. Li and E. Borguet, Determining charge transport pathways through single porphyrin molecules using scanning tunneling microscopy break junctions, *J. Am. Chem. Soc.*, 2011, **134**(1), 63–66.

16 M. L. Perrin, F. Prins, C. A. Martin, A. J. Shaikh, R. Eelkema, J. H. van Esch, T. Briza, R. Kaplanek, V. Kral, J. M. van Ruitenbeek, S. Herre, J. van der Zant and D. Dulić, Influence of the chemical structure on the stability and conductance of porphyrin single-molecule junctions, *Angew. Chem., Int. Ed.*, 2011, **50**(47), 11223–11226.

17 M. L. Perrin, C. A. Martin, F. Prins, A. J. Shaikh, R. Eelkema, J. H. van Esch, J. M. van Ruitenbeek, S. Herre, J. van der Zant and D. Dulić, Charge transport in a zinc–porphyrin single-molecule junction, *Beilstein J. Nanotechnol.*, 2011, **2**(1), 714–719.

18 Z.-F. Liu, S. Wei, H. Yoon, O. Adak, I. Ponce, Y. Jiang, W.-D. Jang, L. M. Campos, L. Venkataraman and J. B. Neaton, Control of single-molecule junction conductance of porphyrins *via* a transition-metal center, *Nano Lett.*, 2014, **14**(9), 5365–5370.

19 M. Lemmer, M. S. Inkpen, K. Kornysheva, N. J. Long and T. Albrecht, Unsupervised vector-based classification of single-molecule charge transport data, *Nat. Commun.*, 2016, **7**, 12922.

20 D. Cabosart, M. El Abbassi, D. Stefani, R. Frisenda, M. Calame, S. Herre, J. van der Zant and M. L. Perrin, A reference-free clustering method for the analysis of molecular break-junction measurements, *Appl. Phys. Lett.*, 2019, **114**(14), 143102.

21 K. F. Cheng, C. Michael Drain and K. Grohmann, Porphyrins linked directly to the 5, 5′ positions of 2, 2′-bipyridine: A new supramolecular building block and switch, *Inorg. Chem.*, 2003, **42**(6), 2075–2083.

22 K. Sonogashira, T. Yasuo and N. Hagihara, A convenient synthesis of acetylenes: catalytic substitutions of acetylenic hydrogen with bromoalkenes, iodoarenes and bromopyridines, *Tetrahedron Lett.*, 1975, **16**(50), 4467–4470.

23 D. K. Dogutan, S. H. H. Zaidi, P. Thamyongkit and J. S. Lindsey, New route to abcd-porphyrins *via* bilanes, *J. Org. Chem.*, 2007, **72**(20), 7701–7714.

24 M. J. Plater, S. Aiken and B. Grant, Metallated porphyrins containing lead (ii), copper (ii) or zinc (ii), *Tetrahedron*, 2002, **58**(12), 2415–2422.

25 O. Robles and F. E. McDonald, Modular synthesis of the c9-c27 degradation product of aflastatin a *via* alkyne-epoxide cross-couplings, *Org. Lett.*, 2008, **10**(9), 1811–1814.

26 P. N. Taylor and H. L. Anderson, Cooperative self-assembly of double-strand conjugated porphyrin ladders, *J. Am. Chem. Soc.*, 1999, **121**(49), 11538–11545.

27 R. Frisenda, D. Stefani, S. Herre and J. van der Zant, Quantum transport through a single conjugated rigid molecule, a mechanical break junction study, *Acc. Chem. Res.*, 2018, **51**(6), 1359–1367.